Variations in the abundances of potassium and thorium on the surface of Mercury: Results from the MESSENGER Gamma-Ray Spectrometer

Patrick N. Peplowski,[1] David J. Lawrence,[1] Edgar A. Rhodes,[1] Ann L. Sprague,[2] Timothy J. McCoy,[3] Brett W. Denevi,[1] Larry G. Evans,[4] James W. Head,[5] Larry R. Nittler,[6] Sean C. Solomon,[6,7] Karen R. Stockstill-Cahill,[3] and Shoshana Z. Weider[6]

Received 25 May 2012; revised 23 July 2012; accepted 24 July 2012; published 3 October 2012.

[1] A technique for converting gamma-ray count rates measured by the Gamma-Ray Spectrometer on the MESSENGER spacecraft to spatially resolved maps of the gamma-ray emission from the surface of Mercury is utilized to map the surface distributions of the elements Si, O, and K over the planet's northern hemisphere. Conversion of the K gamma-ray count rates to elemental abundances on the surface reveals variations from 300 to 2400 ppm. A comparison of these abundances with models for the maximum surface temperature suggests the possibility that a temperature-related process is controlling the K abundances on the surface as well as providing K to the exosphere. The abundances of K and Th have been determined for several geologically distinct regions, including Mercury's northern smooth plains and the plains interior to the Caloris basin. The lack of a significant variation in the measured Th abundances suggests that there may be considerable variability in the K/Th abundance ratio over the mapped regions.

Citation: Peplowski, P. N., et al. (2012), Variations in the abundances of potassium and thorium on the surface of Mercury: Results from the MESSENGER Gamma-Ray Spectrometer, *J. Geophys. Res.*, *117*, E00L04, doi:10.1029/2012JE004141.

1. Introduction

[2] The MErcury Surface, Space ENvironment, GEochemistry, and Ranging (MESSENGER) spacecraft entered into orbit about the planet Mercury on 18 March 2011, inaugurating a one-year primary mission of orbital observations. One of the measurement objectives of the mission has been the characterization of the surface composition of the planet, and to that end the spacecraft carries a suite of geochemical remote-sensing instruments [*Solomon et al.*, 2007]. The MESSENGER Gamma-Ray Spectrometer (GRS), one of two sensors in the Gamma-Ray and Neutron Spectrometer (GRNS) instrument, measures gamma-ray emissions from the surface at energies from 60 keV to 9 MeV [*Goldsten et al.*, 2007]. Initial results from the GRS include relative measurements of the abundances of stable elements, such as Fe, Al, Ca, S, and Na (L. G. Evans et al., Major-element abundances on the surface of Mercury: Results from the MESSENGER Gamma-Ray Spectrometer, submitted to *Journal of Geophysical Research*, 2012, and P. N. Peplowski et al., Aluminum abundance on the surface of Mercury: Application of a new background reduction technique for the analysis of gamma-ray spectroscopy data, submitted to *Journal of Geophysical Research*, 2012), as well as the radioactive elements K, Th, and U [*Peplowski et al.*, 2011b]. Those results are average abundances over the northern hemisphere and contain no information about variations in the elemental composition over the surface.

[3] Simulations of the detector performance carried out prior to orbital insertion suggested that spatially resolved measurements would be possible for the northern latitudes of Mercury following one Earth year of data acquisition [*Peplowski et al.*, 2011a]. Six months of GRS measurements have proven to be sufficient to map variations in measured count rates over the surface for the strongest gamma-ray emitters, including Si, O, and K, the latter of which is extended to a measurement of absolute abundances. Regionally correlated variations in Th are also examined for the purpose of

[1]Johns Hopkins University Applied Physics Laboratory, Laurel, Maryland, USA.
[2]Lunar and Planetary Laboratory, University of Arizona, Tucson, Arizona, USA.
[3]National Museum of Natural History, Smithsonian Institution, Washington, DC, USA.
[4]Computer Sciences Corporation, Lanham-Seabrook, Maryland, USA.
[5]Department of Geological Sciences, Brown University, Providence, Rhode Island, USA.
[6]Department of Terrestrial Magnetism, Carnegie Institution of Washington, Washington, DC, USA.
[7]Lamont-Doherty Earth Observatory, Columbia University, Palisades, New York, USA.

Corresponding author: P. N. Peplowski, Johns Hopkins University Applied Physics Laboratory, 11100 Johns Hopkins Rd., Laurel, MD 20723, USA. (patrick.peplowski@jhuapl.edu)

©2012. American Geophysical Union. All Rights Reserved.
0148-0227/12/2012JE004141

Table 1. Gamma-Ray Photopeaks of Interest for This Work, Along With Their Sources and Relevant Spectral Backgrounds

Element	Gamma-Ray Energy (keV)	Source	Backgrounds[a]
Potassium	1461	Radioactive decay	S_R
Silicon	1779	^{28}Si(n, n′γ) ^{28}Si	S_B, S_N
Oxygen	6129	^{16}O(n, n′γ)^{16}O	S_B, S_N
Thorium	2615	Radioactive decay	S_R

[a] S_R, S_B, and S_N denote spacecraft backgrounds originating from radioactive elements on the spacecraft, GCR-induced gamma-ray production within the spacecraft, and planetary-neutron-induced gamma-ray production within the spacecraft, respectively (see Appendix C for the details).

characterizing the behavior of the K/Th abundance ratio over the surface.

2. Gamma-Ray Spectroscopy

2.1. Sources of Gamma Rays

[4] Gamma-ray emission from a planetary surface arises from both the natural decay of radioactive elements (e.g., K, Th, and U) and the excitation of stable elements (e.g., Si and O) by surface-incident galactic cosmic rays (GCRs) [e.g., *Reedy*, 1978]. The GCR flux consists primarily of protons, but there are small contributions from alpha particles (6–7%) [*McKinney et al.*, 2006] and heavy ions (~1%). GCRs with energies greater than 100 MeV per nucleon interact with atomic nuclei in the surface to produce "fast" (>1 MeV) neutrons through nuclear spallation. These fast neutrons undergo inelastic scattering with nuclei within several hundred g/cm^2 of the surface, exciting them into unstable states that subsequently decay back to stability via the emission of gamma rays at energies that are characteristic of the source element. Fast neutrons also downscatter to thermal energies (<1 eV), where they can be captured by stable elements to produce new isotopes with an additional neutron. The newly created isotopes are typically populated in excited nuclear states that also decay to stable states via gamma-ray emission at characteristic energies. The identification of these gamma rays from orbit allows for the remote characterization of the elemental composition of a planetary surface [e.g., *Prettyman et al.*, 2006; *Boynton et al.*, 2007]. Due to the large mean free paths of neutrons and gamma rays within a planetary surface, gamma-ray spectroscopy is sensitive to elemental composition to depths of tens of centimeters. This depth sensitivity contrasts with other remote sensing techniques, such as X-ray spectroscopy, which is sensitive to composition within 100 μm of the surface.

2.2. MESSENGER Gamma-Ray Spectrometer

[5] The MESSENGER GRS is comprised of two sensitive volumes, a high-purity Ge crystal (HPGe) and a borated plastic scintillator. The scintillator surrounds the HPGe on all sides except the front of the instrument and acts as an anti-coincidence shield by vetoing charged particle and neutron-induced signals originating from GCRs and spallation neutrons generated within the spacecraft. The resulting anti-coincidence spectra have a substantially reduced background continuum and therefore provide a higher signal-to-noise ratio for the gamma-ray peaks of interest. The unshielded front view of the HPGe defines the instrument boresight direction, which is aligned with the instrument deck of the spacecraft and generally faces the planet during periods when the spacecraft is at low altitudes (see Appendix A). Further details on the design and capabilities of the GRS have been given by *Goldsten et al.* [2007].

[6] The GRS is sensitive to incident gamma rays with energies between 0.06 and 9 MeV, a range that includes discrete-energy gamma rays resulting from radioactive decay as well as neutron inelastic scattering and neutron capture reactions. Gamma rays that deposit their full energy in the HPGe produce photopeaks in the GRS spectra. The number of events in these photopeaks, when combined with knowledge of the detector efficiency and measurement geometry, is a direct measure of the gamma-ray flux at the detector. These measurements are compared with models of the surface gamma-ray flux as propagated to the spacecraft altitude in order to determine the abundances of the corresponding elements on the surface. This process is complicated by the highly eccentric orbit of the MESSENGER spacecraft about Mercury (Appendix B). An additional complication arises from the contamination of many of the photopeaks of interest by spacecraft-originating gamma rays. In order to determine the fraction of the measured count rates that originate from the surface, the background contributions for each photopeak must be identified and removed. Table 1 lists the gamma-ray photopeaks used in this study, along with the relevant sources of background (Appendix C).

[7] The gamma-ray flux (φ_γ) measured by the GRS is altitude dependent, varying as

$$\varphi_\gamma = 1 - \sqrt{1 - \frac{{R_M}^2}{(R_M + h)^2}} \quad (1)$$

where h is the altitude of the spacecraft above the surface of Mercury in km and R_M is the radius of Mercury (2440 km). This altitude dependence facilitates the definition of two data-collection regimes of interest: low and high altitudes. Low altitudes are defined to be less than 2000 km, a value that was chosen to maximize the signal-to-noise ratio for the detection of planet-originating gamma rays. The reduced signal-to-noise ratio for data acquired at altitudes greater than 2000 km, coupled with the nature of the MESSENGER orbit about Mercury, limits elemental mapping to northern latitudes [*Peplowski et al.*, 2011a]. High altitudes are defined to be greater than 14,000 km, a value chosen such that the maximum contribution of planet-originating gamma rays to the high-altitude signal is an order of magnitude lower than in the low-altitude spectrum, making the high-altitude spectrum ideal for characterizing non-planetary background signals in the detector.

3. Data Processing

3.1. Data Selection

[8] The analysis in this paper utilized GRS anti-coincidence (AC) spectra collected from orbital observations of Mercury from 24 March 2011 to 28 September 2011. AC spectra were chosen for their optimal signal-to-background ratio for gamma-ray photopeaks. Sub-optimal data were removed from the data set prior to analysis. This includes measurements acquired during orbits with reduced signal-to-noise ratios (e.g., spacecraft-incident solar energetic particle

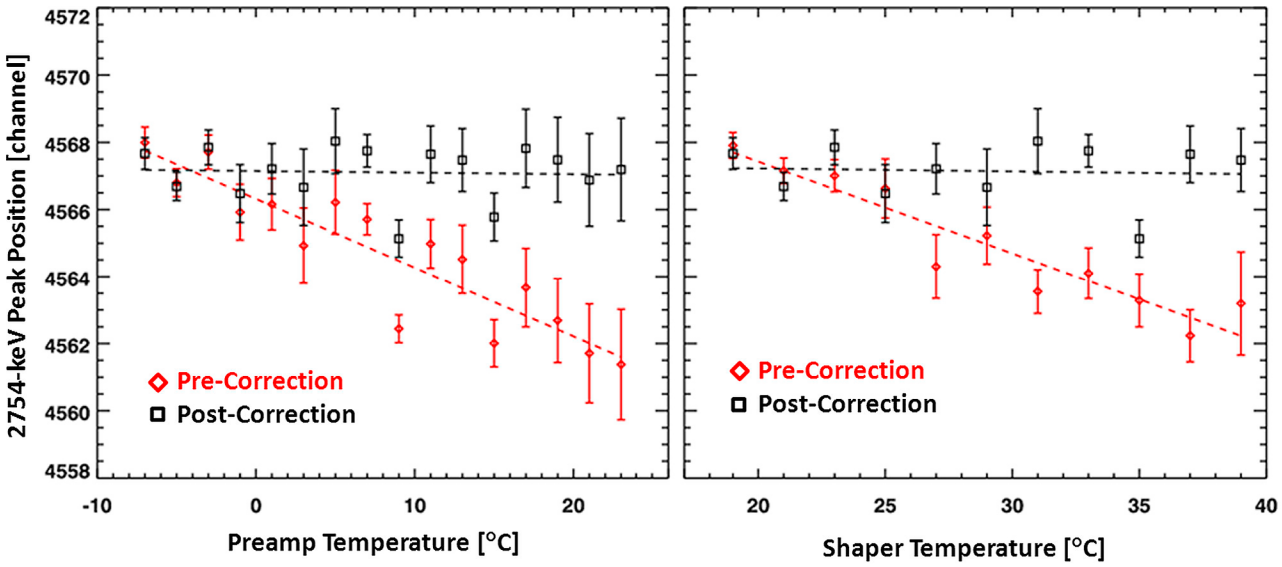

Figure 1. The peak position of the 2754-keV gamma ray plotted versus the temperature of the (left) GRS preamplifier and (right) shaper. Pre-correction data are shown in red, post-correction data (C_T; equation (2)) are shown in black. A linear fit to the temperature-corrected peak positions has a slope of <0.01 keV/°C, indicating that the temperature-dependent gain of the system has been removed.

events) as well as instrument operations activities (e.g., detector annealing).

[9] A further restriction applied to the data set results from spacecraft off-nadir pointing. The gamma-ray detection efficiency of the GRS is a function of the detector-incident angle of the measured gamma rays, primarily as a result of gamma-ray attenuation by spacecraft components surrounding the GRS. In order to remove the most compromised data, measurements taken while the detector boresight was pointed more than 15° away from the sub-nadir position were removed prior to analysis. The remaining orientation-dependent variations in the detector response were corrected in a gamma-ray forward model though the application of a GRS response map (see section 4.4 and Appendix A). Following the application of these restrictions to the data set, the total data acquisition times at low- and high-altitudes are 135 and 1237 h, respectively.

3.2. Energy Calibration

[10] The analysis reported here began with the raw, uncalibrated GRS AC spectra. Each 16,384-channel AC spectrum was calibrated using background gamma rays of known energy (511, 661, 1368, 1809, 2754, and 5616 keV). These gamma rays were chosen for their high count rates and coverage of the energy range of interest. The resulting energy calibration (0.603 keV/channel) was derived from summed high-altitude data and was applied to each spectrum. A second-order correction to the calibration was applied to each spectrum to account for gain shifts resulting from the extreme thermal environment around Mercury, which induces variations of as much as 20°C in the detector pre-amplifier (preamp) and signal shaper temperatures over the course of the mission. Because these electronic units process raw detector outputs prior to analog-to-digital conversion, they are particularly sensitive to temperature variations, and the result of such a variation is a shift in the gain of the output signals (see Figure 1). This effect is removed by applying two empirically derived corrections (C_T) to the energy calibration, one each for the shaper and preamp temperatures:

$$C_T = C_4 \cdot T^4 + C_3 \cdot T^3 + C_2 \cdot T^2 + C_1 \cdot T + C_0 \qquad (2)$$

where the calibration coefficients C_n (n = 0,4) are listed in Table 2 and T is the temperature of the shaper or preamp in °C. The creation of temperature-corrected spectra allows for spectral summing over a wide range of temperatures without degrading the energy resolution of the resulting summed spectrum (see section 3.4).

[11] The full-width half maximum (FWHM) of the temperature-corrected energy spectrum is 4.8 keV at 1369 keV. The increase in the FWHM from the post-launch value of 3.7 keV [*Goldsten et al.*, 2007] is the result of radiation damage to the HPGe crystal accumulated during the 6.6-year interplanetary journey to Mercury. The HPGe was periodically annealed during this period, including immediately prior to

Table 2. Temperature-Correction Coefficients Derived From Ground Tests of the Temperature-Dependent Gain of the MESSENGER GRS

	C_4	C_3	C_2	C_1	C_0
Shaper	9.8926×10^{-12}	7.7979×10^{-10}	-2.5824×10^{-7}	-1.2509×10^{-5}	1.0004
Preamp	-4.5335×10^{-11}	-2.0620×10^{-10}	6.1457×10^{-7}	4.8884×10^{-5}	1.0000

orbit insertion. This annealing process removed some, but not all, of the radiation damage to the crystal.

3.3. Galactic Cosmic Ray Corrections

[12] The source of gamma-ray emission from stable elements is nuclear excitation by surface-incident GCRs (see section 2.1). Analysis of data from previous planetary gamma-ray spectrometers demonstrated a correlation between the time variability of the GCR flux and the measured gamma-ray count rates [e.g., *Lawrence et al.*, 2004; *Maurice et al.*, 2004; *Boynton et al.*, 2007]. To test whether the time-dependent GCR flux drove count rate variations in the MESSENGER GRS data set, the daily, low-altitude 1779-keV Si gamma-ray count rate was compared with an onboard proxy for the GCR flux. Confirmation of a correlation between the measured Si gamma-ray count rate and the GCR proxy would have necessitated the introduction of a GCR correction to the measured stable-element count rates.

[13] There are multiple GRNS measurements that have some degree of sensitivity to the spacecraft-incident GCR flux, but ongoing analysis of data from the Neutron Spectrometer (NS) has demonstrated that the triple-coincidence counter is the most robust. The NS is composed of three sensitive volumes, a borated plastic scintillator located between two adjacent lithium glass scintillators [*Goldsten et al.*, 2007]. These scintillators were designed to detect neutrons through capture reactions on ^{10}B and ^{7}Li, but they are also sensitive to energy deposition by energetic charged particles. When a charged particle is sufficiently penetrating to deposit energy in each of the three detectors, a triple-coincidence event is registered. The geometry of the NS limits such events to those particles originating from a limited portion of the detector field of view, which has an unobstructed view of open space. Radiation transport modeling of charged particles passing through the NS revealed that protons with energy >120 MeV or electrons with energy >20 MeV are required to generate a triple-coincidence signal [*Feldman et al.*, 2010]. Solar energetic particle (SEP) events are the only source of >10 MeV electrons, and GCRs and SEP events are the only source of >100 MeV protons. Since SEP-compromised data have been removed from the data set used for this analysis (section 3.1), the triple-coincidence measurements are a measure of the NS-incident GCR proton flux at energies above 120 MeV. As >100 MeV protons drive the production of neutrons within a planetary surface [*McKinney et al.*, 2006], the triple-coincidence rate is a valid GCR proxy.

[14] The high-altitude (>8000 km), time-dependent NS triple-coincidence rate (Figure 2) exhibits an overall variability of ∼15% during the time period considered here. The high-altitude selection criteria for the triple-coincidence counter results in 17.3 h of data per day, which coupled with the measured count rates (31–37 counts/min) results in a negligible statistical error of ∼0.5% for each daily triple-coincidence measurement. Low-altitude (<2000 km) measurements of the 1779-keV Si gamma ray for the same period exhibit an overall variation of a factor of 3 (Figure 2), and the errors for each value originate from the one-standard-deviation uncertainties in the fitted peak areas (section 3.5). The triple-coincidence measurements are limited to high altitudes to avoid the obscuration of NS-incident GCRs by Mercury, whereas low-altitude Si count rates are used to quantify the changes in the GCR-induced, Mercury-originating signal. The variation in the Si gamma ray count rate is primarily due to the low statistics for daily measurements, although there are also long-term trends in its magnitude.

[15] The daily and weekly averaged 1779-keV Si count rates are plotted versus the corresponding triple-coincidence counter measurements for both data sets in Figure 3. The 1779-keV Si gamma-ray count rate and onboard GCR proxy are not found to be correlated for either the daily or weekly averaged data sets (correlation coefficients of 0.189 and −0.194, respectively). The lack of a correlation between the two measurements negates the need to apply a GCR correction to the data, as any variations due to changes in the incident GCR flux occurred at a magnitude that is smaller than the statistical precision of the Si gamma-ray measurements. Future analysis of MESSENGER GRS data may contain sufficiently low statistical uncertainties to identify and warrant such a correction.

3.4. Spectral Summing

[16] At low altitudes, individual GRS spectra are collected in 60-s integration periods. These spectra do not contain sufficient statistics to be used to characterize the gamma-ray peaks. It is therefore necessary to sum together many spectra over a given region of interest (hereafter referred to as a pixel) to produce a summed spectrum with sufficient statistical significance to characterize the gamma rays of interest. This process is accomplished by summing the optimal, low-altitude, temperature-corrected GRS AC spectra within subsets that correspond to the sub-spacecraft position on the surface during each measurement period. The size of the resulting pixels is determined by the desired statistical significance for each summed spectrum, the details of which are presented in sections 3.6, 4.1, and 4.2 as applied to the characterization of the gamma-ray peaks versus altitude, latitude and longitude, and mapping.

3.5. Gamma-Ray Photopeak Fitting

[17] Determining the total number of events in each gamma-ray photopeak on a pixel-by-pixel basis is the first step in calculating measured gamma-ray count rates as well as the corresponding elemental abundances on the surface. For isolated peaks (e.g., 6129-keV O gamma-ray photopeak and its single- and double-escape peaks), this determination is accomplished by counting the number events in the photopeak that are above the background continuum. Analysis of the 1779-keV Si, 1461-keV K, and 2615-keV Th gamma-ray photopeaks are complicated by the presence of overlapping interference peaks, requiring spectral fitting of these complex regions to isolate the peak areas of interest. Spectral fitting is carried out using exponentially modified Gaussian (EMG) functions [*Felinger*, 1994] with polynomial backgrounds, a procedure that was outlined by *Peplowski et al.* [2011b] and is briefly overviewed here. These fits were carried out with the nonlinear least squares fitting routine MPFIT [*Markwardt*, 2009], which is based on the Levenberg-Marquardt fitting algorithm [*Moré*, 1978]. The one-standard-deviation errors for each fit parameter are calculated from the covariance matrix for each fit.

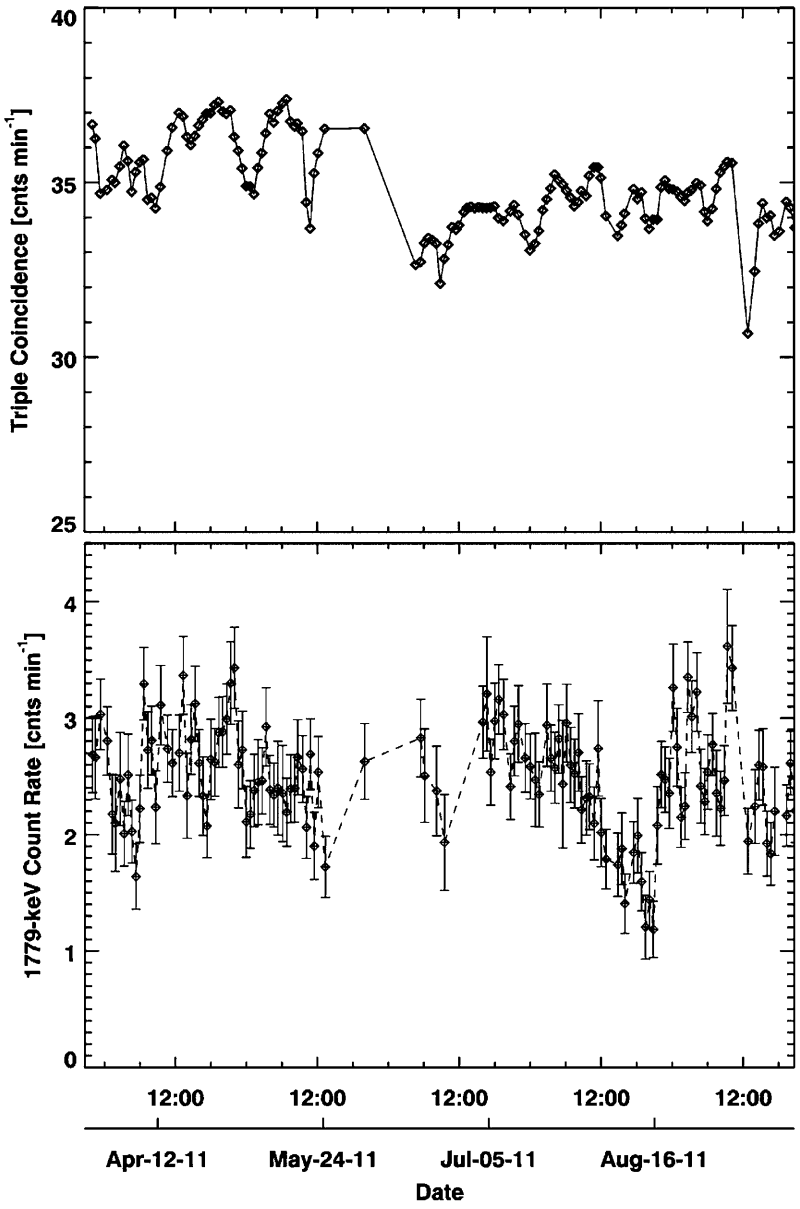

Figure 2. Measurement of the (top) high-altitude triple-coincidence count rate in the MESSENGER Neutron Spectrometer and (bottom) low-altitude 1779-keV Si count rate as a function of time. Triple coincidence requires >100 MeV protons, making it a suitable proxy for the GCR flux at Mercury [*McKinney et al.*, 2006]. With only one exception, the periods of missing triples data correspond to instrument safehold demotions following intense SEP events. These events (e.g., 4 June 2011) frequently drove the short-timescale variability of the local GCR flux, as well as produced pre- and post-flare differences in the GCR baseline value. The errors for the triple-coincidence measurements are sufficiently small (∼0.5%) that they are not included in this figure (see section 3.3).

[18] The EMG function $f(E)$ is

$$f(E) = \frac{A}{2\tau}\left[1 - \mathrm{erf}\left(\frac{\sigma}{\sqrt{2}\tau} - \frac{E_0 - E}{\sqrt{2}\sigma}\right)\right] \exp\left[\frac{\sigma^2}{2\tau} - \frac{E_0 - E}{\tau}\right] \quad (3)$$

where A is the area of the peak in counts, τ is the length of the low-energy tail in keV, σ is the width of the Gaussian peak in keV, E_0 is the peak position in keV, and erf is the error function. The deviation from a pure Gaussian peak shape is the result of radiation damage to the HPGe crystal (section 3.2), which manifests as a low-energy tail.

[19] Multiple overlapping EMG functions were used in regions over which background peaks interfered with the peak of interest. This functional form introduces a large number of free parameters for each fit. A number of procedures were followed to limit the parameter space of the EMG fits, including the use of neighboring, higher-count-rate peaks to constrain τ and σ, as well as the use of starting

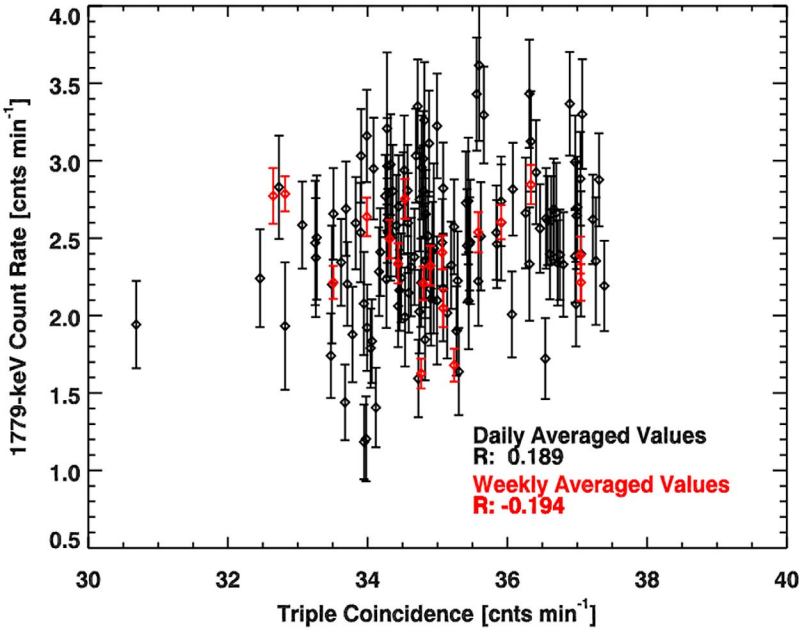

Figure 3. Daily (black) and weekly (red) summed low-altitude 1779-keV Si gamma-ray count rate plotted versus the corresponding high-altitude NS triple coincidence count. The low correlation coefficient (R) demonstrates that GCR-correlated variations in the 1779-keV Si gamma ray are not observed within the statistical uncertainties of the measurements, and so a GCR correction to MESSENGER GRS data is not warranted at this time. The errors for the triple-coincidence measurements are sufficiently small that they are not included in this figure or in the calculation of the correlation coefficient R (see section 3.3).

parameters that were based on fits to summed spectra having lower statistical errors that are scaled by the relative integration times. For example, the high-count-rate 1809-keV gamma-ray peak was used to constrain the τ and σ parameters for the fit to the peaks in the 1779-keV region, and the starting parameters were derived from fits of the entire low-altitude spectrum scaled by the fraction of the integration time for the pixel of interest to the total low-altitude data set.

[20] Fitted peak areas were corrected for the channel size (0.603 keV/channel), data integration period, and detector dead time to produce the measured high- and low-altitude gamma-ray count rates for each peak, along with the one-standard-deviation statistical errors. Examples of the peak fits for Si, K, and Th are shown in Figure 4, and the results are summarized in Table 3 for the high- and low-altitude data sets. The high-altitude measurements are used to define the background contributions to the low-altitude GRS measurements. For the 1461-keV K and 2615-keV Th gamma rays, the high-altitude measurements quantify the spacecraft-originating backgrounds resulting from K and Th contamination in the spacecraft. Subtracting these from the low-altitude measurements results in a determination of the planet-originating signal. For the 1779-keV Si and 6129-keV O gamma rays, the high-altitude measurements quantify the GCR-induced backgrounds. This background varies with the altitude of the spacecraft, and subtracting the high-altitude value multiplied by the altitude-dependent fraction of the spacecraft field of view that is not obscured by Mercury removes this contribution from the low-altitude measurements (see section 3.6 and Appendix C). These background corrections were applied to all data used in the following sections.

3.6. Solid-Angle Correction

[21] The dominant source of variation in the low-altitude gamma-ray count rates is the altitude of the spacecraft (equation (1)). These variations have the potential to mask smaller effects such as compositional heterogeneity on the surface and must be removed by correcting for the altitude-dependent solid angle, $\Omega(h)$, of the measurements. $\Omega(h)$ is defined as the fraction of the 4π-sr unit sphere around the GRS that is subtended by the horizon-to-horizon field of view of the planet as seen by the instrument and is calculated from

$$\Omega(h) = \frac{\int_0^{2\pi}\int_0^{\theta\max} \sin\theta \, d\theta \, d\varphi}{\int_0^{2\pi}\int_0^{\pi} \sin\theta \, d\theta \, d\varphi} = \frac{1 - \cos\theta_{\max}(h)}{2} \quad (4)$$

where the angle from the spacecraft sub-nadir point to the horizon ($\theta_{\max}$) is

$$\theta_{\max}(h) = \operatorname{acos}\left[\frac{\left[(R_M + h)^2 - R_M{}^2\right]^{1/2}}{(R_M + h)}\right] \quad (5)$$

The geometry of the solid angle and its relationship to the spacecraft altitude are discussed in Appendix A. For the purpose of comparative studies of the abundances of elements on the surface, the relative solid angle $\Omega_R(h)$ is defined to be

$$\Omega_R(h) = \frac{\Omega(h)}{\Omega(2000\ \text{km})} \quad (6)$$

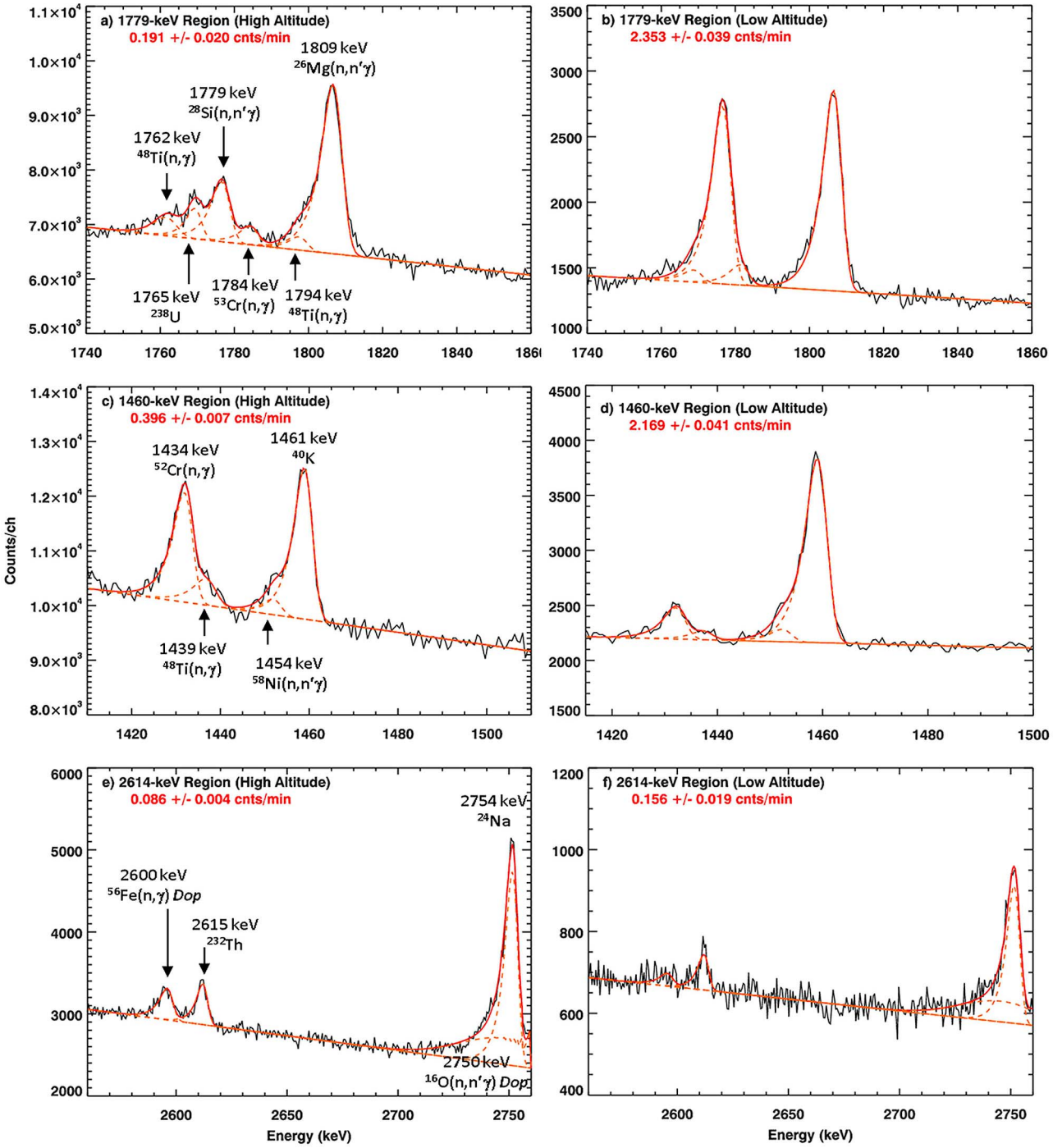

Figure 4. High- and low-altitude peak fits for near-nadir ($\theta_n \leq 15°$) GRS measurements of the (a and b) 1779-keV Si, (c and d) 1461-keV K, and (e and f) 2615-keV Th gamma rays as well as neighboring and interfering peaks that are included to ensure good fits to the entire region. Peak energies and sources are listed in the high-altitude spectra (Figure 4, left) and are based on the identifications by *Evans et al.* [2006]. *Dop* indicates the peak is Doppler broadened.

Dividing the background-corrected gamma-ray count rates by $\Omega_R(h)$ serves to normalize the data to an effective measurement altitude of 2000 km, the highest altitude permitted in this data set. The upper limit of 2000 km was chosen to prevent measured count rates from being inflated by corrections. The statistical errors are not scaled by the solid angle, which prevents errors from being improperly reduced by the solid-angle correction.

[22] The background-corrected 1779-keV Si, 6129-keV O, and 1461-keV K gamma-ray count rates versus solid angle are shown in Figure 5, both before and after $\Omega_R(h)$ is applied. The 6129-keV count rate value includes the

Table 3. High-Altitude (>14,000 km) and Low-Altitude (<2,000 km) Peak Areas for the Gamma Rays Analyzed in This Work[a]

Element	Gamma-Ray Energy (keV)	High-Altitude Count Rate (cnts/min)	Low-Altitude Count Rate (cnts/min)
Potassium	1461	0.396 ± 0.007	2.169 ± 0.041
Silicon	1779	0.191 ± 0.020	2.353 ± 0.039
Oxygen	6129	0.289 ± 0.004	1.783 ± 0.014
Thorium	2615	0.086 ± 0.004	0.156 ± 0.019

[a]Low-altitude data are restricted to nadir-pointing ($\theta_n \leq 15°$) measurements only. Peak areas are limited to the full-energy photopeaks, with the exception of the 6129-keV oxygen data, which include counts from the first- and second-escape peaks.

summed contributions from both the single and double escape peaks (5618- and 5107-keV, respectively), each of which has a peak area that is comparable to the photopeak. Prior to making the $\Omega_R(h)$ correction, each gamma ray count rate increases with increasing solid angle as expected. Following the correction, the Si and O gamma rays exhibit uniform count rates versus solid angle, whereas K still exhibits variation. The nature of the MESSENGER orbit results in a correlation between the solid angle and the latitude of the measurement (see Appendix B), and therefore Figure 5c is suggestive of latitude-dependent variations in the 1461-keV K planetary gamma-ray emissions.

4. Gamma-ray Count Rate Variations

4.1. Count Rate Versus Latitude and Longitude

[23] An initial search for compositional heterogeneity was carried out by investigating variations in the measured count rate as a function of latitude and longitude with the data analysis procedure outlined above. The statistical significance of the photopeaks determined the size of the pixels in latitude and longitude. Latitudinal sums were created with low-altitude, southbound data only, as these data have lower altitudes over the northern hemisphere and a corresponding higher spatial resolution than the GRS data acquired during the northbound portion of the orbit. Longitudinal sums were created with low-altitude, northbound data, which have lower spatial resolution but more complete coverage in longitude at small nadir angles. The resulting count rates are shown in Figure 6. Statistically significant variations in the 1461-keV count rate as a function of latitude (Figure 6e) are observed, with an overall variability of a factor of 3. Longitudinally correlated variations in the K abundance are also observed (Figure 6f). These results contrast with the measured 1779-keV Si and 6129-keV O count rates, which do not show statistically significant variations in latitude or longitude at the two-standard-deviation level.

4.2. Count Rate Mapping

[24] Gamma-ray count rate maps were created following the data analysis procedure outlined above. The resulting maps (Figure 7) show the measured gamma-ray count rates on a scale of zero to twice the average count rate, facilitating a direct comparison of the relative variations for all three gamma-ray count rates. Pixel sizes vary with latitude and were chosen to limit the maximum statistical error per pixel. The Si gamma-ray count rates have one-standard-deviation uncertainties of ≤15% over the entire map, with the majority of the uncertainties near 10%. The oxygen gamma-ray count rates have uncertainties of 15 to 20% over the entire surface. The K gamma rays have uncertainties of ≤10% for regions north of 45°N, and larger uncertainties for the southernmost pixels as a result of the lower count rates in those regions. These maps confirm the results of Figures 5 and 6, which indicate that the Si and O gamma-ray count rates do not show statistically significant variations over the surface at the two-standard-deviation level. This result contrasts with the K gamma-ray count rates, which exhibit large, statistically significant variations over the surface.

4.3. Abundance Mapping

[25] Converting the measured 1461-keV gamma-ray count rates to an elemental abundance map for K requires the application of a forward code to propagate the known ^{40}K gamma-ray decay rates at the surface per unit abundance to the flux at the position of the orbiting GRS. Application of the principles of radioactive decay, in conjunction with the known half-life of ^{40}K ($t_{1/2} = 1.248 \times 10^9$ yr), its isotopic abundance (0.0117%), and its probability for emitting a 1461-keV gamma ray (10.66%), yields a flux at the surface of 19.6 cnts min^{-1} cm^{-2} per wt% K [*Peplowski et al.*, 2011b]. The surface flux was propagated to the spacecraft for each 60-s GRS integration period in the data set to determine the flux per wt% at the spacecraft altitude. This flux was multiplied by the attitude-dependent cross-sectional area of the GRS, then corrected for the detection efficiency at 1461-keV (see Appendix A) to yield the expected count rate per wt% K. Dividing the measured count rate in each pixel by the corresponding calculated count rate per wt% K yielded a map of K abundances on the surface of Mercury (Figure 8). To maximize the coverage of the surface, pixels of varying size were used to increase the spatial coverage without reducing the statistical significance of the measurements.

[26] The K map shows a large variation in the elemental abundance over the surface, with a dynamic range of 300 to 2400 ppm. The highest abundances are found in the far northern regions, although high values extend southward at longitudes of ±90°. Correlations between the K abundances and large-scale geologic provinces (see Figure 8) are discussed in section 5.1. Measurements of the near-equatorial

Figure 5. Measured count rates plotted as a function of solid angle for the (a) 1779-keV Si, (b) 6129-keV O, and (c) 1461-keV K gamma rays, before (red) and after (black) applying the solid-angle correction $\Omega_R(h)$. The vertical scales for each figure range from zero to two times the average count rate prior to the $\Omega_R(h)$ correction, facilitating comparisons of the relative variations for all three elements. The dashed lines indicate the average post-correction count rate and are included to highlight the relative variations around this value. Figures 5a and 5b exhibit the expected dependence of gamma-ray count rate on solid angle, and after correction they exhibit no solid-angle dependence. The residual variation with solid angle in the post-correction K count rate (Figure 5c) suggests a non-uniform abundance of K on the surface.

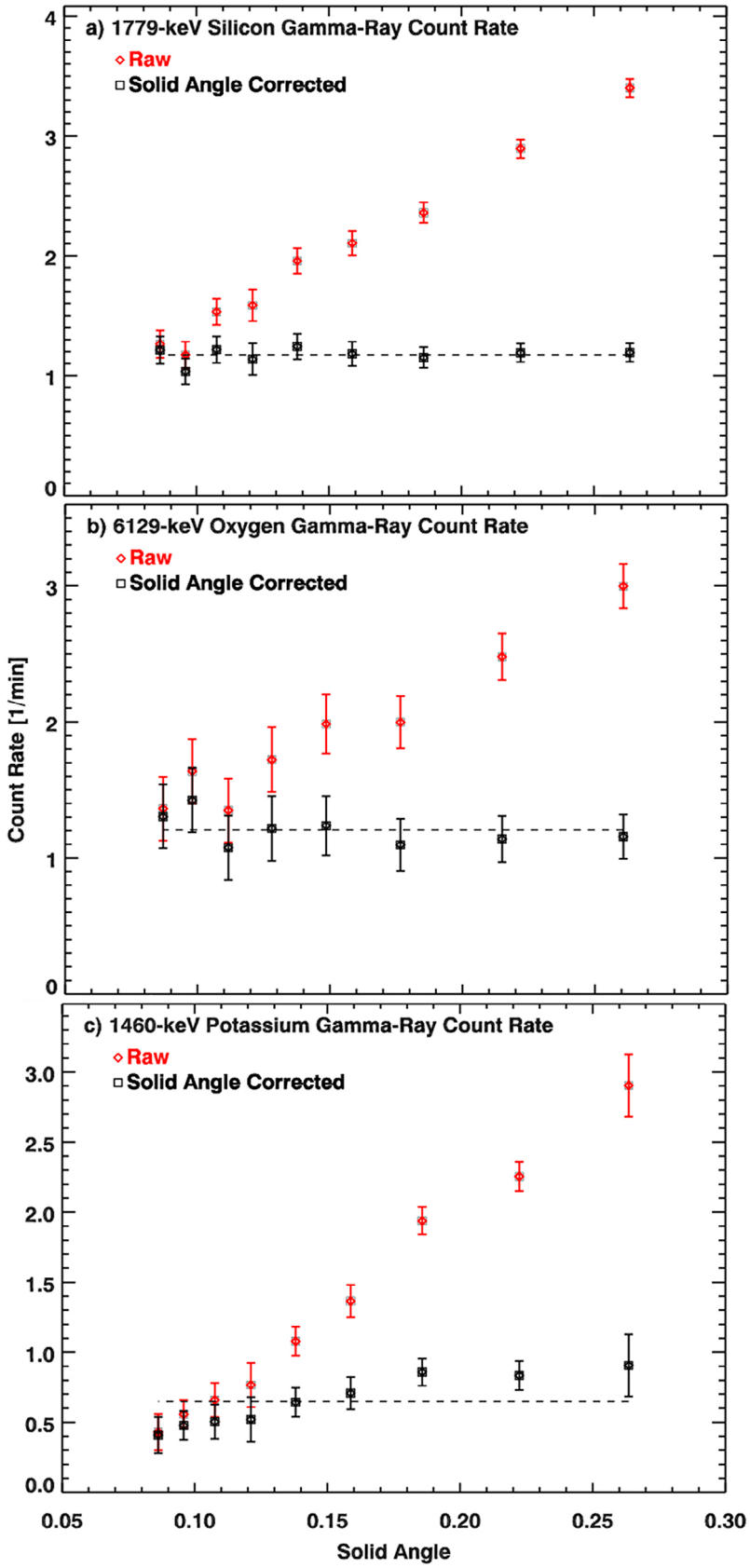
a) 1779-keV Silicon Gamma-Ray Count Rate
Raw
Solid Angle Corrected
b) 6129-keV Oxygen Gamma-Ray Count Rate
Raw
Solid Angle Corrected
c) 1460-keV Potassium Gamma-Ray Count Rate
Raw
Solid Angle Corrected
Count Rate [1/min]
Solid Angle
0.05
0.10
0.15
0.20
0.25
0.30

Figure 5

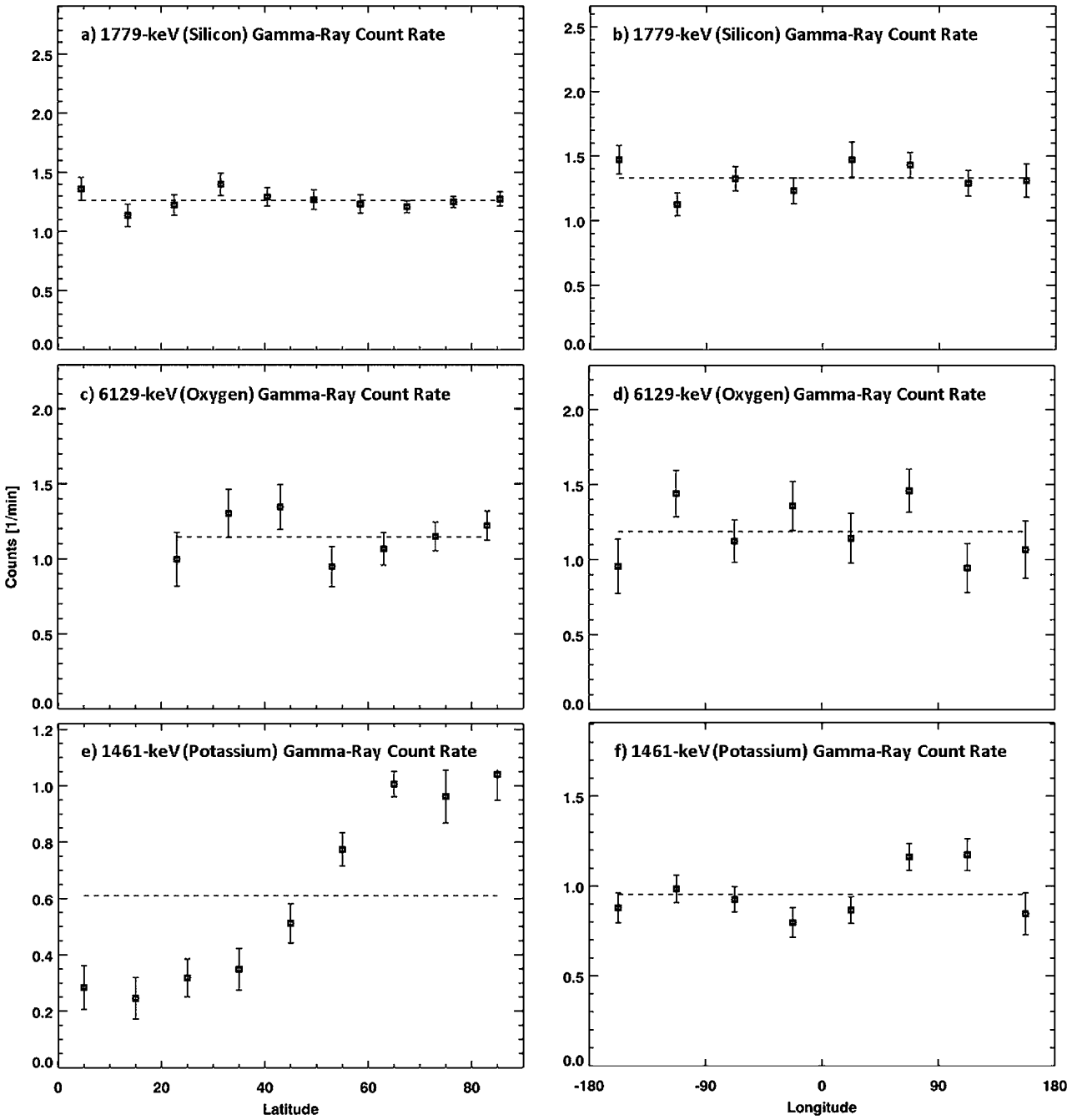

Figure 6. Measured count rates for (a and b) 1779-keV Si, (c and d) 6129-keV O and escape peaks, and (e and f) 1461-keV K as functions of (left) latitude and (right) longitude. The vertical scales for each figure range from zero to two times the average count rate, facilitating comparisons of the relative variations for all three elements. Latitudinal data are limited to the southbound portions of each orbit, ensuring the highest spatial resolution possible. Longitudinal data are restricted to northbound data, to ensure full coverage over all longitudes, and are further restricted to data acquired between latitudes 40° and 90°N. The errors represent one-standard-deviation statistical uncertainties. The K gamma-ray count rate shows large, statistically significant variations over the surface, particularly as a function of latitude, which contrasts with the Si and O gamma-ray count rates, which are uniform within their uncertainties.

abundance of K with Mercury flyby GRS data were published by *Rhodes et al.* [2011], and their results (870 ± 360 ppm) are consistent with the elemental abundances derived in this work for comparable regions.

4.4. Thorium Abundances

[27] The low measured count rates for Th gamma rays do not permit the creation of a Th map with spatial resolution and statistical significance comparable to those for the K

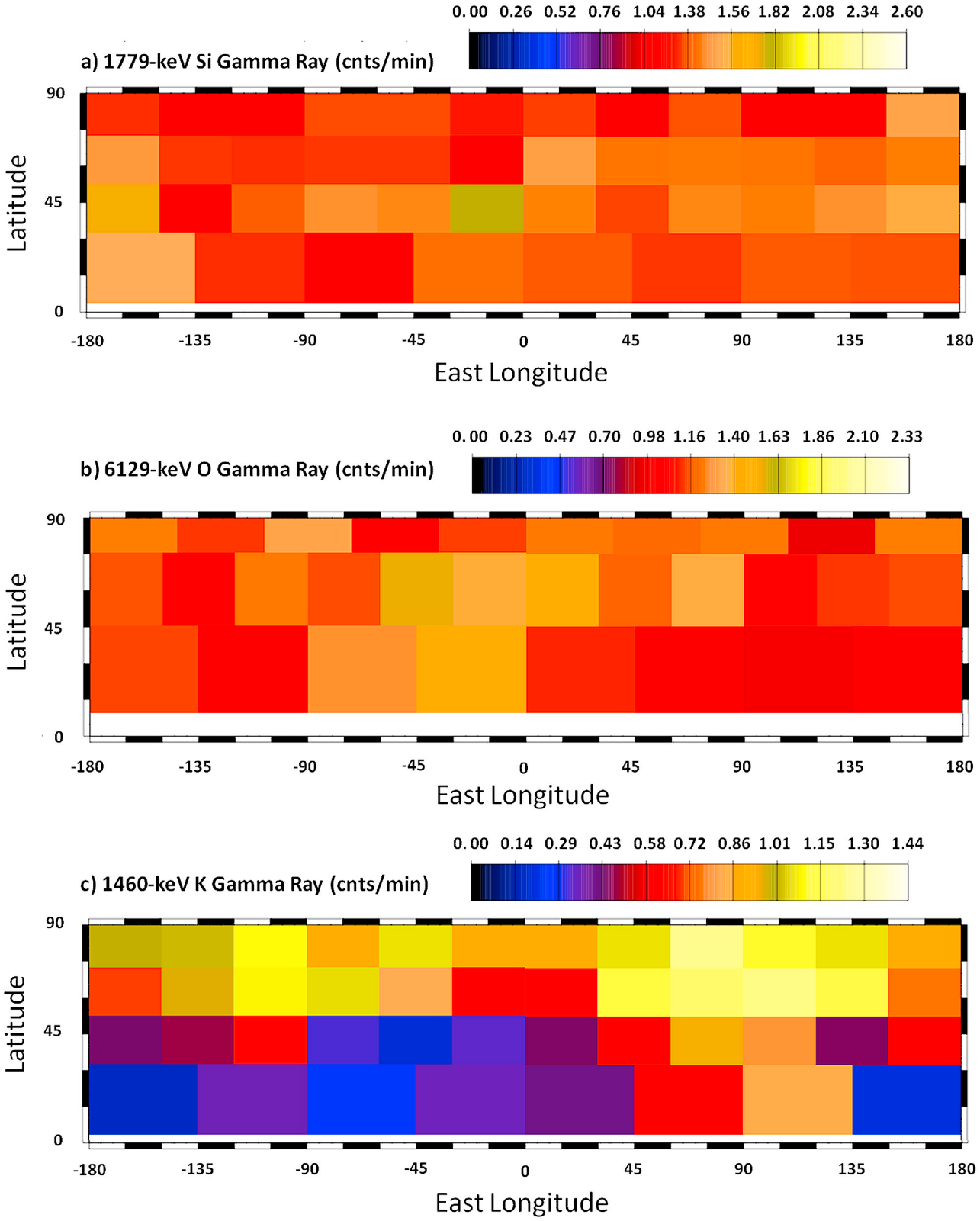

Figure 7. Maps of solid-angle-corrected gamma-ray fluxes originating from (a) Si, (b) O, and (c) K at varying spatial resolution in the northern hemisphere of Mercury. The color scales for each map range from zero to two times the average count rate, facilitating comparisons of the relative variations for all three elements. Variations in the K count rate (about a factor of 4) are substantially larger than those for Si and O (±20%).

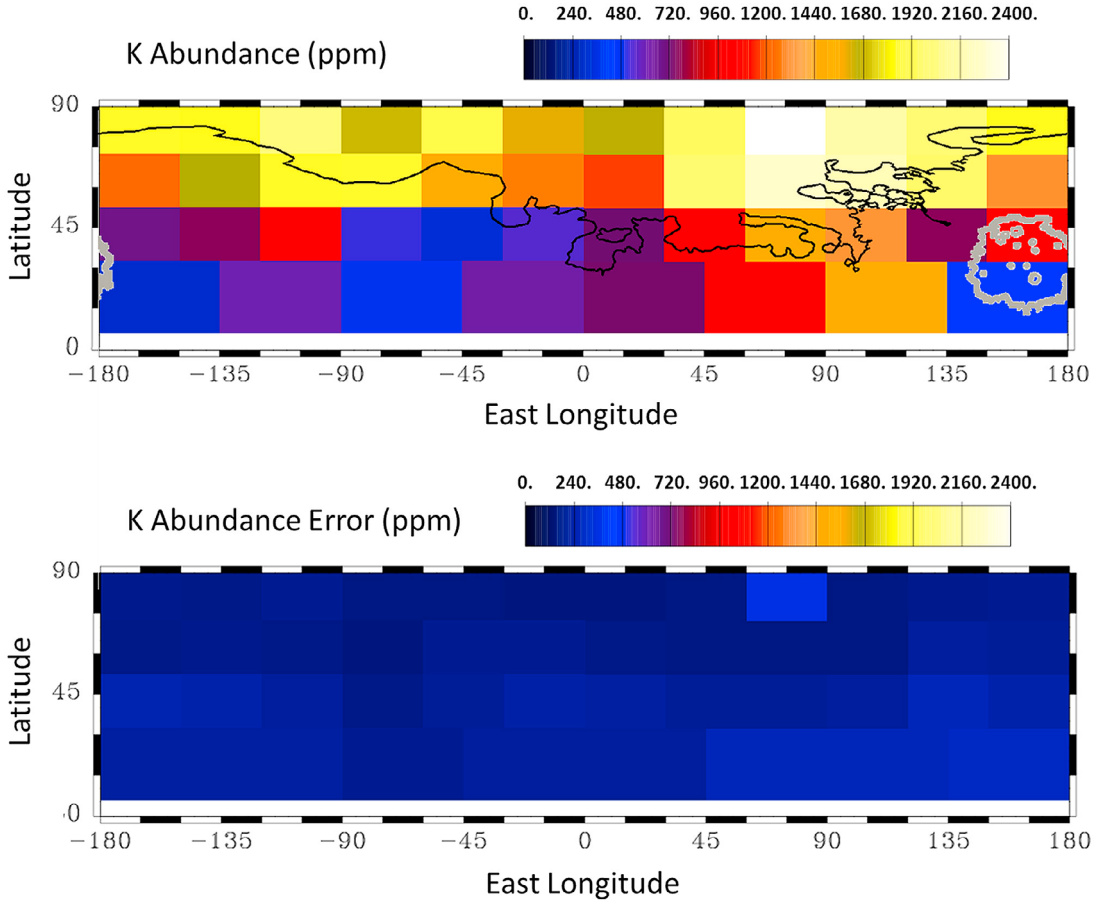

Figure 8. (top) Map of abundance of K on the surface of Mercury and (bottom) the one-standard-deviation statistical errors per bin. On the abundance map are outlines of the northern volcanic plains (black) and the high-reflectance plains material inside the Caloris basin (gray).

map, but sufficient data exist to determine the Th abundances within large, geologically distinctive regions. For these calculations, each pixel represents the total area of the geologic unit of interest (Figure 8), and all spectra that were acquired while the sub-spacecraft point was within these regions contribute to the sum. The 2615-keV gamma-ray count rate for each pixel was converted to a Th elemental abundance following the procedure outlined in section 4.3, and the results are listed in Table 4. Due to the large footprint of the GRS over the surface, the summed spectra contain contributions from regions outside of the geologic units considered here, and therefore the abundances listed in Table 4 also contain contributions from surrounding regions. Overall, Th is not found to vary over the surface at the one-

Table 4. K and Th Abundances From GRS Data Collected Over Selected Areas on Mercury[a]

	Planetary Count Rate		Modeled Count Rate		Abundances		
Region	K (1461 keV) (cnts/min)	Th (2615 keV) (cnts/min)	K (1461 keV) (cnts/min/wt%)	Th (2615 keV) (cnts/min/wt%)	K (ppm)	Th (ppm)	K/Th
All 2011[b]	1.266 ± 0.056	0.066 ± 0.024	11.0 ± 2.0	3768 ± 490	1150 ± 220	0.175 ± 0.064	6600 ± 2800
All 2012	1.432 ± 0.035	0.059 ± 0.019	11.1 ± 2.0	3805 ± 494	1288 ± 234	0.155 ± 0.054	8000 ± 3200
NVP	2.527 ± 0.105	0.069 ± 0.036	14.1 ± 2.5	4871 ± 633	1786 ± 330	0.142 ± 0.075	13000 ± 7100
CB	0.776 ± 0.155	0.190 ± 0.095	10.3 ± 1.9	3517 ± 633	754 ± 203	0.540 ± 0.288	1400 ± 800
IcP/HCT/SP	0.976 ± 0.041	0.059 ± 0.023	10.3 ± 1.8	3504 ± 630	952 ± 176	0.168 ± 0.072	5700 ± 2600

[a]All denotes all sampled areas, NVP denotes the northern volcanic plains, CB denotes the Caloris basin interior, and HCT/ICP/SP denotes the sampled regions outside of the NVP and CB, which includes heavily cratered terrain (HCT), intercrater plains (IcP), and smooth plains (SP) as applied by *Weider et al.* [2012]. IcP/HCT/SP, although not a geologically distinct region, was chosen to test the hypothesis that the NVP is distinct from its older surroundings in its K abundance. The results from *Peplowski et al.* [2011b], included here (All 2011) for comparison, were derived from the first 59 days of orbital data. For an equivalent comparison of the All 2012 values to All 2011, the former values were calculated without the nadir-angle restriction of $\theta_n \leq 15°$ for this data set only. The errors are the one-standard deviation statistical and systematic errors; for a discussion of the systematic errors of MESSENGER GRS measurements, see *Peplowski et al.* [2011b].

[b]The thorium abundance and K/Th ratio from *Peplowski et al.* [2011b] were derived from the 2615-keV peak only (see section 4.4).

standard-deviation level with the exception of the Th abundance for the Caloris basin interior, which is found to be 1.3 standard deviations larger than the northern-hemisphere average value.

[28] Unlike the analysis of *Peplowski et al.* [2011b], this analysis does not utilize the 911-keV gamma ray in the Th abundance calculation. That earlier work was based on the assumption that the 911-keV line originated entirely from Th for both the spacecraft-originating background and the planetary signal, a view supported by modeled planetary gamma-ray fluxes [*Reedy*, 1978] as well as previous analyses [e.g., *Evans et al.*, 2006]. Analysis of the behavior of the high-altitude 911-keV gamma ray as a function of time has identified an increase in its count rate and a change in its spectral shape following the solar particle event of 4 June 2011. The change in shape includes a shift in the peak position to lower energy (~908 keV). As 911-keV Th gamma-ray emission is not excited by incident charged particles, these observations suggest that there is a previously unidentified source of 908-keV gamma rays originating from the excitation of spacecraft materials by incident charged particles. The low signal-to-noise ratio of the 911-keV Th peak makes spectral fitting challenging in this region, and the added complication of a time-dependent interfering peak at 908 keV adds large uncertainties to any Th abundance derived from the 911-keV peak. As a result, this peak has not been utilized in our determination of the Th abundance.

[29] The data used by *Peplowski et al.* [2011b] were collected prior to the 4 June 2011 event, so the post-flare increase in the 911-keV count rate was not a factor in that analysis. However, the presence of a 908-keV background in the post-flare data raises the possibility that non-flare-compromised data also included contributions from an unknown 908-keV source of gamma rays. This uncertainty introduces the prospect that the Th abundances derived from this gamma ray result in an overestimation of the planetary Th abundances. *Peplowski et al.* [2011b] found that the Th abundance derived from the 911-keV peak was larger than that derived from the 2615-keV peak, but the two values were consistent to within the errors of the measurements, and the final reported Th abundance was the average of the two values. In light of the possibility that there is an interfering peak in the 911-keV region, the *Peplowski et al.* [2011b] Th abundance derived from both the 2615- and 911-keV gamma rays (0.220 ± 0.060 ppm) was replaced by their value from the 2615-keV peak of 0.175 ± 0.070 ppm for the discussion in this paper (Table 4). The K/Th ratio of 5200 ± 1800 was likewise replaced by the value derived from the 2615-keV peak of 6600 ± 2800.

5. Potassium on the Surface of Mercury

5.1. Correlations With Major Geologic Units

[30] The observed variations in K over the surface of Mercury invite a comparison to the known geologic units on the surface. As the spatial resolution of the GRS is ~1000 km over the mapped regions, only large geologic units are included in this comparison. These units include the northern volcanic floodplains that cover 6% of the total surface area of the planet [*Head et al.*, 2011] as well as the smooth plains interior to the 1,550-km-diameter Caloris impact basin. Outlines of these units are shown on the K abundance map in Figure 8. There is no clear correlation between the observed K abundances and the locations of these units, but the northern volcanic plains are generally higher in K than other regions. Analysis of orbital data from the MESSENGER X-ray Spectrometer (XRS) by *Weider et al.* [2012] demonstrate that the northern volcanic plains are also compositionally distinct (in terms of Mg, Al, S, and Ca) from the surrounding older terrain. A limited number of XRS measurements of the Caloris basin reveal an elemental composition for the interior basin plains that is similar to the composition of the northern volcanic plains unit, a result that is consistent with their similar spectral reflectance and color properties [*Denevi et al.*, 2009]. This similarity contrasts with the measured K abundances, which differ significantly between the northern volcanic plains and the Caloris basin interior. The plains interior to Caloris do not appear as a distinct region in the K abundance map. This result runs contrary to the interpretation of ground-based mid-infrared measurements that the Caloris basin interior plains have spectral features indicative of particularly high abundances of K-rich feldspar [*Sprague et al.*, 2009].

[31] To quantify possible correlations between the K abundance map and the geologic units discussed here, K abundances were calculated for subsets of the coverage area corresponding to the geologic regions of interest following the procedure outlined in section 4.4. As is the case for the regional Th measurements, the large footprint of the GRS on the surface results in the calculation of abundances from observations that include contributions from outside the regions of interest. As a result, the calculated abundances do not strictly correspond to the listed regions. Even with this complication, the results (Table 4) reinforce the conclusion that the northern volcanic plains are predominantly contained within the region of higher K. The Caloris basin interior has the lowest average K abundance of the regions considered, although it is within one standard deviation of the average abundance for the older terrain surrounding the northern volcanic plains.

5.2. Potassium- to-Thorium Ratio

[32] The abundances of relatively volatile elements on the surface of Mercury, including K, have important implications for our understanding of the formation and early evolution of the planet [e.g., *Taylor and Scott*, 2003]. GRS measurements of the present-day elemental composition of the surface can be used to test the validity of formation models for Mercury through a comparison with their predicted surface compositions. Processes that have modified modern abundances from their original values complicate these comparisons. For example, Mercury's surface has been subject to extensive volcanic activity [e.g., *Head et al.*, 2008], and volcanic processes are known to modify the abundances of incompatible elements such as K and Th. To avoid this complication, the ratio of the abundance of the moderately volatile K to that of Th, a refractory element, is frequently used as a proxy for the volatile inventory of a planet [e.g., *Prettyman et al.*, 2006; *Taylor et al.*, 2006]. On the Moon and Mars, the measured K/Th ratio is observed to be nearly constant over the surface, despite large regional variations in the absolute values for each element. This near uniformity is due to the incompatible nature of these elements during

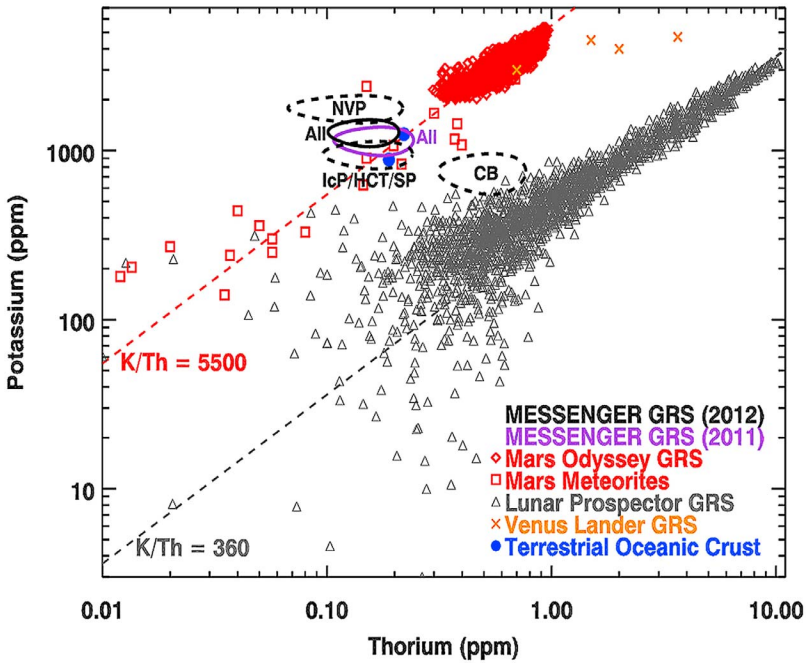

Figure 9. K abundances plotted against Th abundances for Mercury [*Peplowski et al.*, 2011b], the Moon [*Prettyman et al.*, 2006], Mars [*Taylor et al.*, 2006], Venus [*Surkov et al.*, 1987], and Earth [*Lodders and Fegley*, 1998]. Measurements of spatially resolved abundances of K and Th corresponding to GRS data collected when the spacecraft sub-nadir point was within the boundaries of the northern volcanic plains (NVP), Caloris basin (CB), and regions outside of the NVP and CB (denoted IcP/HCT/SP, see Table 4) are also included and suggest the possibility of variations in K/Th over the surface of Mercury (see Table 4). The ellipses for K and Th abundances on Mercury represent the one-standard-deviation statistical and systematic errors of the measurements. Values originate from both orbital gamma-ray spectroscopy (GRS) and laboratory measurements (see legend). Lines of constant K/Th for the Moon and Mars are shown for comparison. The K/Th value for Mercury is found to be consistent with that of Mars and an order of magnitude larger than for the volatile-depleted Moon, suggesting that Mercury is not depleted in volatiles. The absolute abundances agree with the values from Martian meteorites and terrestrial oceanic basalts, both of which represent products of partial melting of mantle material depleted in incompatible elements from volatile-rich planets.

partial melting, as both concentrate in the melt phases; and the K/Th ratio in volcanic material tends to reflect the ratio in the mantle source region of those magmas.

[33] Abundances of K (1150 ± 220 ppm) and Th (175 ± 68 ppb; see section 4.4), along with the K/Th ratio (6600 ± 2800; see section 4.4) for Mercury were reported by *Peplowski et al.* [2011b] as globally averaged values for all regions northward of 20°S. These values are consistent with the northern-hemisphere average K and Th abundances obtained in this analysis (Table 4). A comparison of the K and Th abundances for Mercury to those for the Moon, Mars, Venus, and Earth is shown in Figure 9. The agreement between the Mercury northern-hemisphere averaged K/Th ratio to that of Mars (K/Th ∼ 5500), which is an order of magnitude larger than the volatile-depleted Moon (K/Th ∼ 360), were found to be inconsistent with the predictions of most of the pre-MESSENGER formation theories for Mercury [e.g., *Taylor and Scott*, 2003] that called for extreme heating of the planet or its precursor materials [*Peplowski et al.*, 2011b]. *McCubbin et al.* [2012] have questioned the inference of a volatile-rich Mercury from the K/Th ratio, but this conclusion was supported by the discovery of higher than expected abundances of the volatile element S by the MESSENGER XRS [*Nittler et al.*, 2011] and the geologic evidence for recent volatile-related activity on the surface [*Blewett et al.*, 2011]. Additional evidence is found in the high Na abundance presented in a companion paper by Evans et al. (submitted, 2012).

[34] The regional K and Th abundances (Table 4) derived in this work are also included in Figure 9 for the purpose of characterizing the behavior of the K/Th ratio over the surface. The ratio for each region is distinct from the others at the one-standard-deviation level. These differences raise the possibility that the K/Th ratio is not constant over Mercury's surface, in contrast to the general situation on the Moon and Mars (see section 5.3). Alternatively, a secondary process may have modified the abundance of one or both of these elements at Mercury's surface (see section 5.4).

5.3. The K/Th Ratio at Low Th Abundances

[35] Following *Peplowski et al.* [2011b], we compare in Figure 9 MESSENGER GRS measurements of the K and Th abundances on Mercury to orbital gamma-ray measurements of the surfaces of the Moon and Mars. These orbital gamma-ray spectrometer measurements, and the derived K/Th ratios, are biased toward regions with higher abundances of these

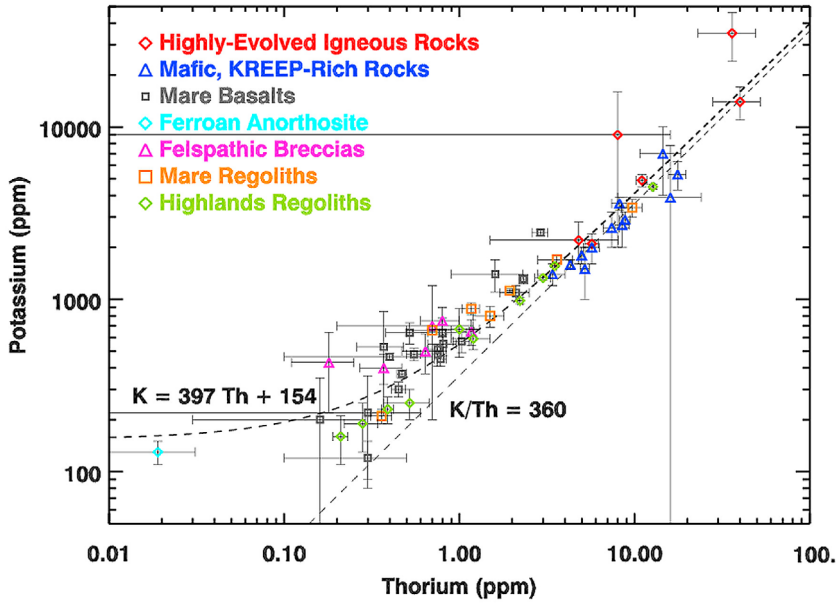

Figure 10. K abundance versus Th abundance for a wide range of lunar samples as compiled by *Korotev* [1998]. At high K and Th abundances, the data are consistent with a constant K/Th ratio similar to that (360) inferred from remote-sensing gamma-ray measurements. However, at the lowest Th abundances, similar to those observed on Mercury, the K/Th ratio values diverge from the ratio at higher abundances. The error bars represent the 95% confidence limits for each category and reflect both the number of measurements and variance of the average values (see *Korotev* [1998] for details).

elements. Examination of the K and Th abundances measured by Lunar Prospector for the pixels with the lowest K and Th values reveal considerable deviation from a line of constant K/Th. As the statistical uncertainty of these values is larger than for the regions with higher abundances, it is not readily apparent as to whether this spread is the result of the precision of the measurements or the properties of the surface.

[36] The extensive collection of lunar samples, whose elemental abundances are well known, can be used to examine the behavior of the K/Th ratio over a wide range of K and Th abundances with a higher precision than is possible for the orbital gamma-ray spectrometer measurements. The elemental abundances compiled by *Korotev* [1998] are used as the basis for this analysis, and the formalism utilized in that paper is also adopted here. This formalism includes grouping the lunar samples into seven categories; highly evolved igneous rocks (IR); mafic, KREEP-rich rocks (KR); mare basalts (MB); ferroan anorthosites (FA); feldspathic breccias (FB); mare regolith samples (MR); and highland regolith samples (HR). A plot of K versus Th abundances for these samples is shown in Figure 10.

[37] The highest K and Th abundances in the lunar samples are found in the IR and KR categories, which correspond to the most highly processed material on the lunar surface. The large K and Th abundances found in these materials are the result of interior melting, which concentrated these incompatible elements. The IR and KR abundances closely follow the Lunar-Prospector-derived K/Th ratio of 360 (Figure 10). The least processed materials are the FA and HR samples, which are more representative of the earliest lunar crust, albeit modified by subsequent impact processes. These samples exhibit considerable spread in their K and Th abundances and deviate systematically from the K/Th ratio derived from samples with higher K and Th abundances. *Korotev* [1998] found that the relationship between K and Th was best described as

$$K = 397\ Th + 1547 \quad (7)$$

where K and Th are the elemental abundances in ppm. For large Th abundances, this relation reduces to a K/Th ratio of 397, close to the value of 360 adopted by *Taylor et al.* [2006] and utilized by *Peplowski et al.* [2011b].

[38] Of particular interest for comparison to Mercury is the behavior of K in the regime of low Th abundances. For a Th abundance of 0.2 ppm (close to Mercury's value), the K abundances of the lunar samples vary from 100 to 700 ppm (Figure 10), a dynamic range that is similar to the observed range on Mercury. To the extent that these data sets can be applied to Mercury, they suggest that in the limit of low Th the generality of constant K/Th may break down. Similarly, the Martian meteorites with the lowest Th abundances also appear to deviate from the average K/Th value (Figure 9), although this deviation occurs at Th abundances of <0.05 ppm, which is lower than those found on Mercury.

[39] The K and Th abundances on Mercury are in good agreement with those for terrestrial oceanic basalts and the Martian meteorites with the higher K and Th abundances (Figure 9), both of which represent partial melting products of mantle depleted in incompatible elements. That the Martian meteorites with similar K and Th abundances to Mercury follow the global K/Th ratio derived from Mars Odyssey GRS data [*Boynton et al.*, 2007] (Figure 9) despite low absolute abundances of K and Th relative to surface material suggest that measurements of mantle material

depleted in incompatible elements may still be valid for inferring the global K/Th ratio. The difference between the behavior of the K/Th ratio for lunar and Martian samples with Th abundances of ~0.2 ppm likely result from the different origins of these materials, as the lunar samples represent material formed during magma ocean crystallization whereas the Martian samples represent products of partial melting of depleted mantle. The evidence for extensive volcanic material on the surface of Mercury suggests that the Martian meteorites may be better analogues for understanding the K/Th ratio in the limit of low Th.

5.4. Relation to Surface Temperature

[40] The comparatively volatile nature of K, along with the possibility that a secondary process may be modifying the K/Th ratio on the surface (section 5.2), raises the question of whether surface temperature may play a role in modifying the near-surface abundances of K. To test this hypothesis, the distribution of measured K abundances was compared with models of the maximum temperature [*Vasavada et al.*, 1999] reached at depths comparable to the sensitivity of gamma-ray spectroscopy (≤ tens of centimeters). The profile of surface temperature on Mercury results in a bimodal distribution of maximum values centered at the equator and at 0° and 180° longitudes, collectively termed Mercury's hot poles [*Soter and Ulrichs*, 1967]. These hot poles are the result of the relatively large eccentricity of Mercury's orbit around the Sun coupled with its 3:2 spin-orbit resonance, which places these longitudes at local noon during alternating perihelia. The maximum surface temperature at a depth of 7 cm (Figure 11) was compared with the GRS-derived K abundance map (Figure 8) by measuring the correlation coefficient R between the two parameters (Figure 12) both for all temperatures as well as just those above 350 Kelvin (see section 6). The R values (−0.82 and −0.84, respectively) suggests a high probability that the K abundance is anti-correlated with the maximum surface temperature. This anti-correlation is also observed for the temperature at depths of 0 and 15 cm.

[41] If temperature-driven processes are modifying the surface K abundances, then two possibilities present themselves. K may be preferentially lost to the exosphere, which is known to have a measurable K component (section 6), resulting in a permanent loss of K from the surface. Alternatively, the dominant effect may be that K is redistributed to the surface in cooler polar regions. In the first case, the present K abundances provide an underestimate of the planetary K/Th ratio. In the second case, the northern-hemisphere average values presented here and by *Peplowski et al.* [2011b] may be a valid representation of the global value since this scenario does not result in a net loss of K from the planet, although the GRS-derived elemental abundances are determined under the assumption of a uniform composition within the depth sensitivity of gamma-ray spectroscopy (upper tens of centimeters). If near-equatorial K is being redeposited in the polar regions only within a thin veneer, then the K abundances presented here may overestimate the actual values.

[42] The existence of a veneer of K that is biasing the GRS-measured K abundances is considered unlikely, however, in the presence of regolith gardening, a process that continually overturns near-surface material through repetitive small impacts. For the 1461-keV K gamma ray in regolith with a Mercury-like composition [*Nittler et al.*, 2011; *Peplowski et al.*, 2011b; Evans et al., submitted, 2012], 90% of the surface gamma-ray flux originates from the top 20 cm of the regolith, and 50% originates from the top 6 cm. Lunar regolith overturn timescales for the top 6 cm are 10^7–10^8 y per complete overturn with a probability of 50–99% [*Hörz et al.*, 1991]. On the basis of scaled meteoroid influxes, *Killen et al.* [2007] estimated that the timescale for regolith overturn on Mercury is 0.15 times the lunar value, which leads to an estimate of 10^6-10^7 y per overturn and a total of 10–100 overturns over the age of Mercury. As Mercury's 3:2 spin-orbit resonance is stable [*Colombo and Shapiro*, 1966; *Goldreich and Peale*, 1966], it is unlikely that the thermal conditions at the hot poles have appreciably changed on a timescale that is shorter than that for regolith overturn. As a result, if near-equatorial K is being redeposited in the polar regions, the resulting veneer has been well mixed within the top tens of centimeters of the regolith and is therefore not biasing GRS measurements of the K abundance.

[43] The observed correlation between the K abundance and the maximum surface temperature offers a possible explanation for observation that the XRS-measured composition of the Caloris basin and the northern volcanic plains are similar [*Weider et al.*, 2012], whereas they differ significantly in their K abundances. Given that the Caloris basin interior plains are volcanic in origin [*Watters et al.*, 2009], the material may have originally been enriched in incompatible elements such as K and Th. The position of Caloris basin near one of Mercury's hot poles, however, may have depleted the near-surface K but would have left the Th abundance comparatively unaltered. This explanation also accounts for the unusually low K/Th abundance ratio for this region (Figure 9 and Table 4), which is found to be considerably lower than the other regions examined here.

6. Implications for the Exosphere

[44] The results of section 5.3 suggest that the relatively low K concentrations measured by the GRS near Mercury's hot poles might be the result of thermally driven diffusion of K out of near-surface regolith to the gas–surface interface, where it is then lost to the exosphere or transported to polar regions. One likely host mineral for K (and the volatile Na also observed in the exosphere) is alkali-bearing feldspars. Diffusion rates in feldspars have been measured at temperatures of 600–1000 Kelvin [*Giletti and Shanahan*, 1997]. A linear extrapolation of these diffusion rates to 300–500 Kelvin suggests that 10 μm grains would lose K on timescales of about 500,000 yr at 500 Kelvin. Even grains approaching 1 mm in size would lose K in several billion years. However, 10 μm grains would require timescales greatly exceeding the age of the Solar System to lose K at 300 Kelvin. These differences in the diffusion rate are fully consistent with the observed relationship between the measured K abundances and maximum surface temperatures (Figure 12) could therefore account for the loss of K from equatorial regions and its retention in cooler polar regions.

[45] Any ejection mechanism, such as thermal desorption [*Sprague*, 1990, 1992] or diffusion-limited photodesorption [*Killen et al.*, 2004], can populate the exosphere. *Domingue et al.* [2007] provided a thorough discussion of release

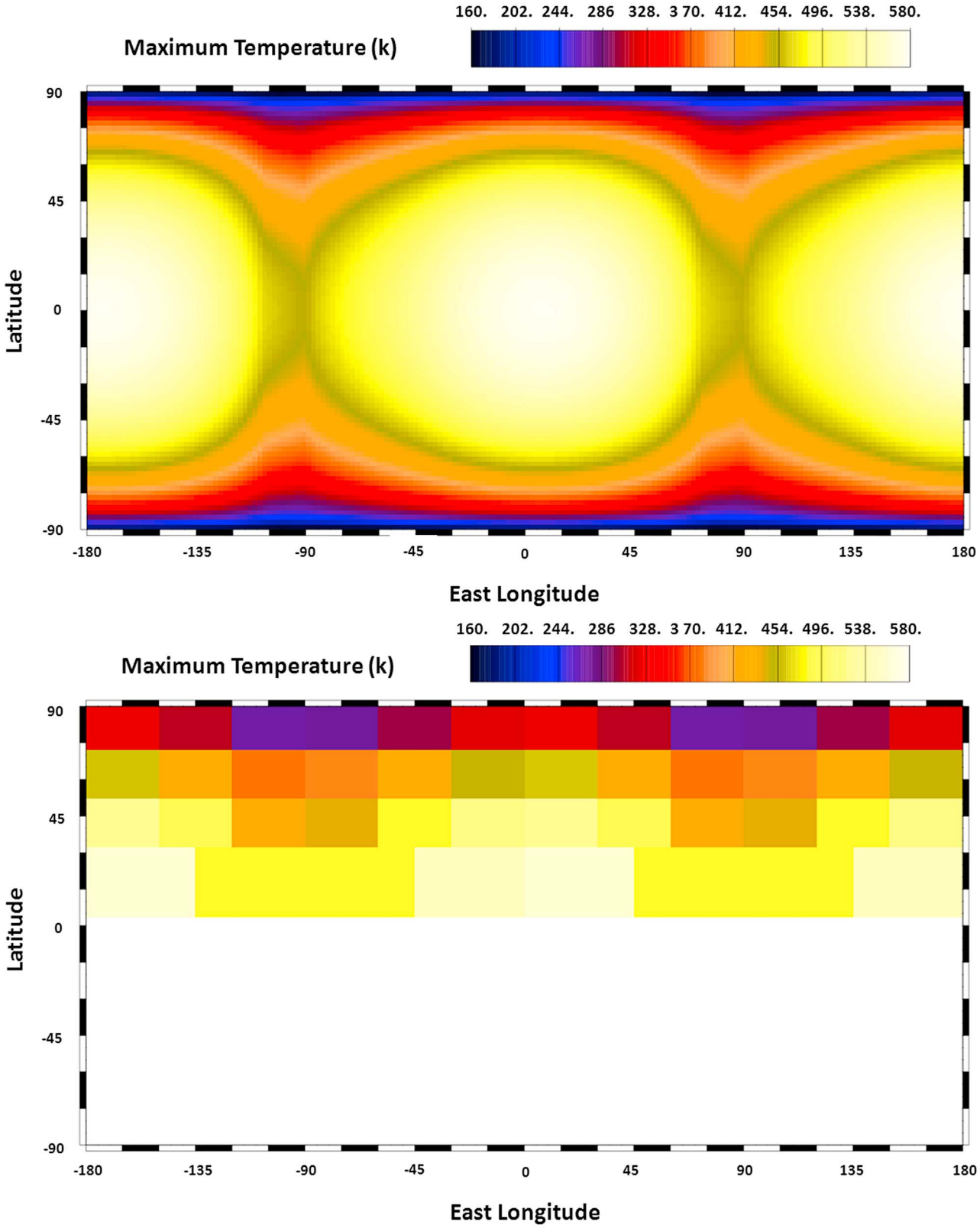

Figure 11. (top) Maximum temperature at 7 cm depth on Mercury (D. A. Paige, personal communication, 2012) derived with the formalism of *Vasavada et al.* [1999]. This model does not include surface topography. The hot poles (0° and 180° longitude) have the highest average surface temperatures. (bottom) Maximum temperature at a spatial resolution equivalent to that of the K abundance map in Figure 8, with regions outside of the GRS coverage area (latitude <5°) removed.

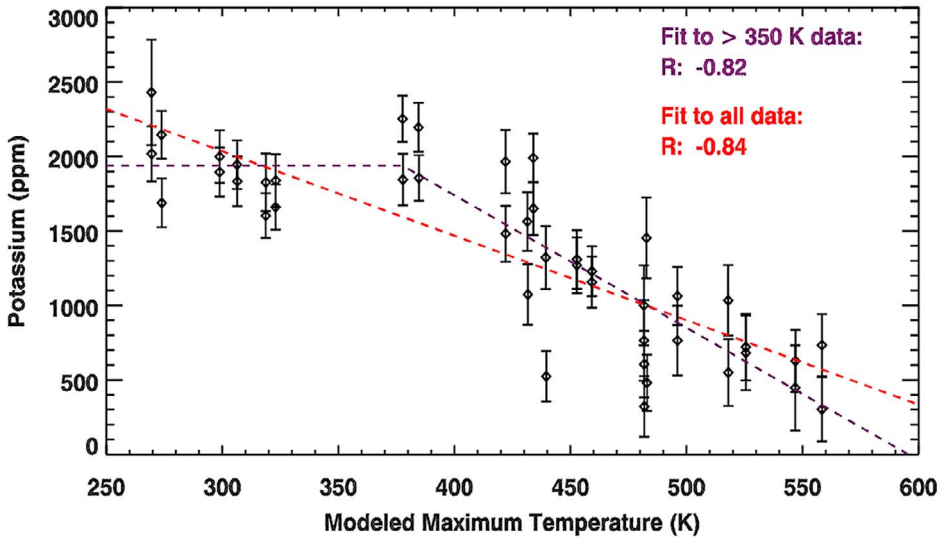

Figure 12. Measured K abundances versus the modeled maximum temperature at a depth of 7 cm (Figure 11) for each pixel in Figure 8. A linear fit of K abundance as a function of the maximum temperature was carried out over all temperature ranges (red), and the correlation coefficient (R) of −0.84 indicates a high likelihood that the two quantities are related. A separate fit (purple) was carried out under the assumption of no correlation between K abundance and maximum temperature for regions at low (<350 Kelvin) maximum temperature but a linear relationship at higher temperatures, consistent with the discussion of temperature-driven diffusion of K presented in section 6. For the latter scenario, the correlation coefficient at high temperatures is −0.82, again indicating a strong correlation between the two variables.

mechanisms. The hypothesis that K is preferentially mobilized to the surface and added to the exosphere at warm latitudes and longitudes would result in diminished abundances in the top ∼30 cm of the regolith, which is of the order of the depth sensitivity of the GRS measurements. In such a scenario, equatorial regions and particularly areas near the hot poles gradually lose K relative to cooler longitudes and higher-latitude regions, consistent with the distribution of K on the surface (Figure 8).

[46] Once atoms are part of the exosphere, they become visible through resonant scattering emissions. Telescopic measurements by *Potter and Morgan* [1986] yielded estimates of the Na/K ratio in the exospheres of Mercury and the Moon to be ∼14 and 5, respectively. Subsequent measurements indicated that the Na/K ratio in Mercury's exosphere varies from 20 to 190, with the minimum value corresponding to that near the sub-solar point. This pattern has been attributed to the fact that the photo-sputtering rate of K is twice that of Na and the lifetime against ionization is ∼6.9 times longer. Observations also showed that at Mercury the Na abundance exceeds that at the Moon by a factor of ∼250, whereas K at Mercury exceeds the lunar value by ∼93. These inferences, along with the measurements by *Sprague et al.* [1990] indicating more than an order of magnitude enhancement of exospheric K at "warm longitudes" and equatorial and middle latitudes than at other locations, led *Sprague* [1990] to suggest a diffusion source for Na and K at Mercury and the Moon. Mercury's higher temperature and the strong temperature dependence of diffusion could account for the ratios of Na to K without requiring markedly different Na and K abundances in surface rocks and regoliths on the two bodies.

[47] The observations of *Potter and Morgan* [1997] showed that K in Mercury's exosphere is spatially and temporally variable, with indications that K might be sputtered from surface materials at high latitudes. *Doressoundiram et al.* [2010] measured Na and K simultaneously at Mercury over an extended time period in 2006 and found that the Na/K ratio varied with true anomaly. They also observed the dawn enhancement of K first noted by *Sprague* [1992], again indicating a strong mobilization of K by thermal processes. *Leblanc and Doressoundiram* [2011] assembled all available Mercury exospheric measurements of K and compared them with models that include temperature-driven diffusion and evaporation, photo- and electron desorption, and ion sputtering. Also included in the simulations were the effects of radiation pressure on atoms and the thermal effects of Mercury's eccentric orbit. Thermally driven flux rates are sufficiently high to contribute a major fraction of the observed K and Na exospheric components. Their results indicate that a substantial fraction of the surface reservoir for K is driven by diffusion from subsurface materials, consistent with the observed correlation between the maximum near-surface temperature and the GRS-measured K abundances.

7. Conclusions

[48] MESSENGER GRS measurements of the surface composition of Mercury demonstrate that the abundance of K varies from 300 to 2400 ppm over the surface in the northern hemisphere. There is no clear relation between K

abundance and large-scale geologic terrain types, but such a comparison is complicated by the low spatial resolution of the GRS measurements. Overall, the northern volcanic plains are contained within an area having the highest K abundances, and Caloris basin is located within a region of low K abundances. In contrast, the Th abundance does not vary resolvably over the surface, although the statistical errors are large for individual regions. If Th abundances do not vary appreciably, then the K/Th ratio on the surface is not constant. This finding runs contrary to expectations from orbital measurements on the Moon and Mars, but K/Th in lunar samples at low Th abundances is found to depart systematically from the nearly constant ratio seen at higher abundance values. It is also possible that variations of K/Th on Mercury may be the result of a secondary process that modifies the K abundance. This prospect is supported by an anti-correlation of K abundance with maximum predicted surface temperature, a result suggesting that K near the equator and particularly near Mercury's hot poles is being mobilized and lost to the exosphere, redistributed to polar regions, or both. If so, the distributions of K on the surfaces of the Moon and Mars should not be used to guide our interpretations of the observed K abundances on Mercury, as the maximum surface temperatures on these bodies are not sufficient to appreciably deplete K within the age of the solar system.

Appendix A: Efficiency of the MESSENGER GRS

A1. Gamma-Ray Spectrometer Coordinate System

[49] Converting measured count rates to the gamma-ray flux at the detector requires detailed knowledge of the energy- and attitude-dependent detection efficiency of the GRS. This knowledge includes both the intrinsic efficiency of the detector as well as the attenuation of the signal by spacecraft components surrounding the instrument. A combination of pre-launch calibration measurements and radiation transport modeling were used to characterize the response of the GRS. The coordinate system for these measurements is outlined in Figure A1. In the detector-fixed coordinate system, θ_D is the angle between the boresight direction and gamma-ray incidence, and ϕ_D describes the rotation of θ_D around the HPGe axis of symmetry. In the spacecraft-planet reference frame, the nadir angle θ_n is the angle between the spacecraft z-axis and the spacecraft-to-planet-center vector. The spacecraft z-axis is parallel to but offset from the GRS boresight, but because this offset is much smaller than the distance between the spacecraft and the surface, θ_D and θ_n are considered equivalent. The azimuthal angle ϕ_n describes rotations of the spacecraft around its z-axis and is similarly analogous to ϕ_D.

A2. Ground Calibration

[50] Prior to launch, the detection efficiency for incident gamma-ray energies ranging from 239 keV to 9717 keV was characterized during a series of ground calibration measurements made with both calibrated gamma-ray sources (^{60}Co, ^{226}Ra, and ^{228}Th) and neutron capture reactions on Cr and Cl targets utilizing a reactor cold-neutron beam [*Goldsten et al.*, 2007]. Measurements were taken at angles of θ_D = 0°, 22.5°, 45°, and 67.5° and a wide range of azimuthal angles ϕ_D to characterize the variation in gamma-ray detection efficiency as a function of the gamma-ray incident angle. Figure A2 illustrates just one example of the ground

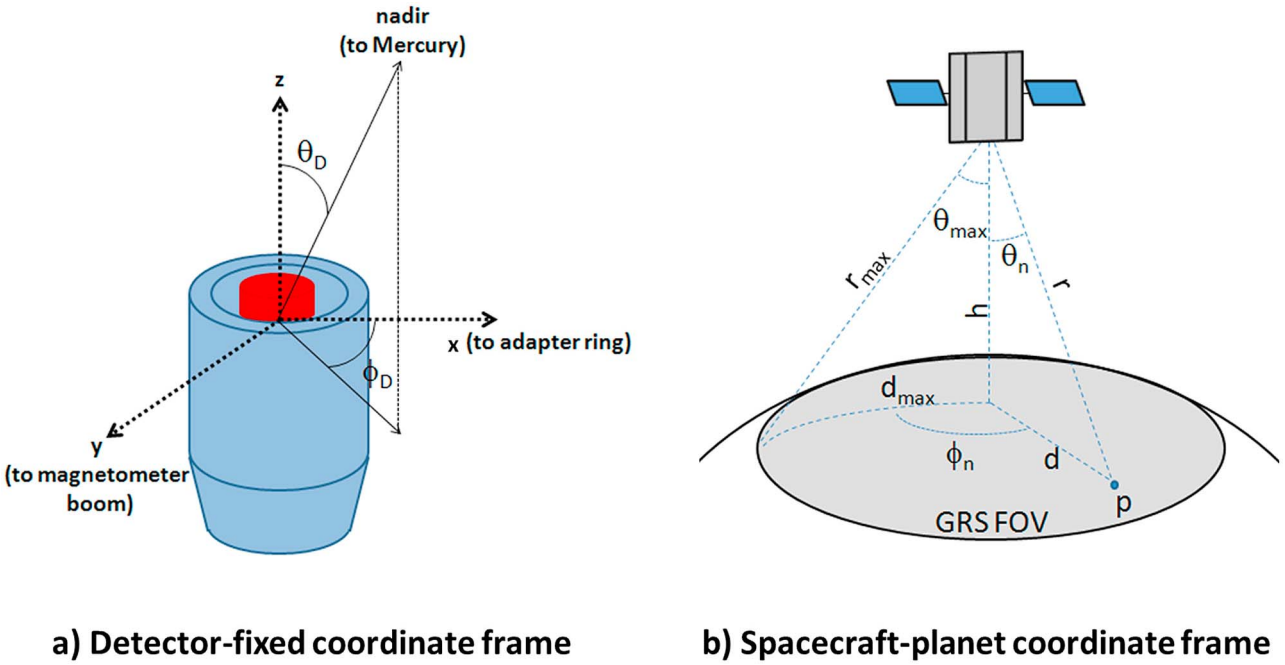

Figure A1. (a) Detector-fixed and (b) spacecraft-planet coordinate systems used in this analysis. Figure A1a details the active detector elements, with red showing the high-purity germanium (HPGe) sensor and blue showing the plastic scintillator anti-coincidence shield. The placement of the detector on the spacecraft is illustrated in Figure A3.

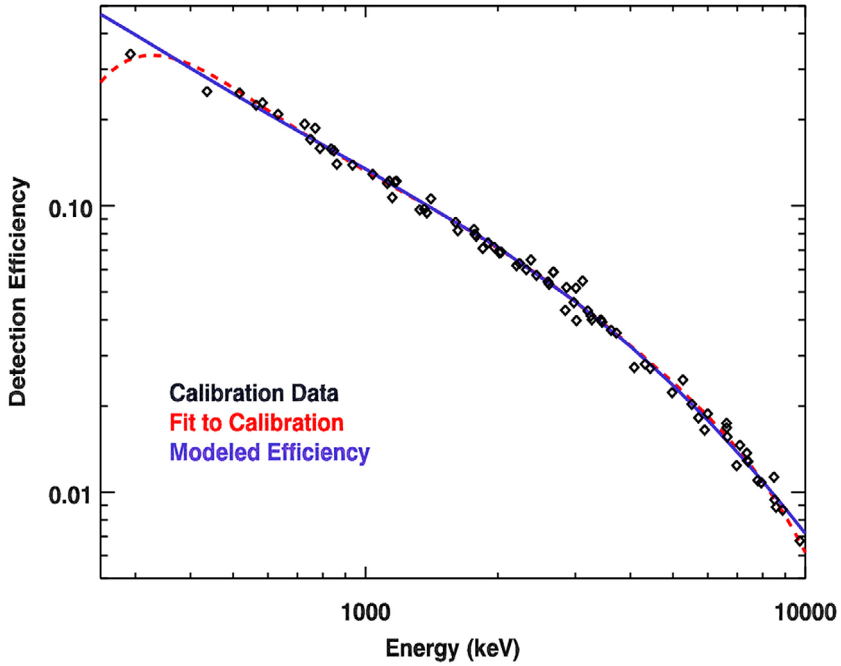

Figure A2. A comparison between the $\theta_D = 0°$ ground calibration measurements of gamma-ray photopeak detection efficiency and the Geant4-simulated detector response. The close agreement between these values, as well as ground calibration data taken at $\theta_D = 22.5$, 45, and 67.5° for a wide range of ϕ_D values, validated the simulations, which were extended to create maps of the efficiency for arbitrary energy and incidence angle (e.g., Figure A4).

calibration measurements and the sixth-degree polynomial fit of $\ln(\varepsilon)$ versus $\ln(E_\gamma)$ that describes energy-dependent detection efficiency at this orientation, where ε is the intrinsic detection efficiency and E_γ is the gamma-ray energy. Despite the large number of ground calibration measurements that were taken, they cover only a limited range of the total relevant gamma-ray incidence angles, necessitating the use of radiation transport modeling to create an efficiency map for the GRS at arbitrary incident energies and angles.

A3. Modeled Response

[51] The radiation transport modeling code Geant4 [*Agostinelli et al.*, 2003] was used to model the response of the GRS. Geant4 has a heritage of space-based applications; for example, it was applied toward modeling the efficiency of the Gamma-ray Spectrometer on the SELENE lunar mission of the Japan Aerospace Exploration Agency [*Kobayashi et al.*, 2010]. A custom Geant4 application was created to model the efficiency of the MESSENGER GRS, using original computer-aided design (CAD) drawings to reproduce the dimensions and material compositions of the instrument. The simulations were benchmarked with the ground-calibration measurements at hundreds of different gamma-ray energies and incident angles. The results of a subset of these simulations are shown in Figure A2. A 4% reduction in the dimensions of the HPGe crystal was required to match the $\theta_D = 0°$ ground calibration measurements, probably originating from the fact that the active volume of the crystal was slightly smaller than its total volume. Following this correction, the simulations were found to agree with the ground calibration measurements to within 5% for all $\theta_D > 0°$ measurements without further modification to the detector geometry. This agreement facilitated the expansion of the simulations to model the detector response for arbitrary gamma-ray energies and incident angles, including the effects of gamma-ray attenuation by GRS-surrounding spacecraft components.

[52] The FASTRAD toolkit [e.g., *Pourrouquet et al.*, 2011] was used to import the CAD geometries of the spacecraft components and instruments surrounding the GRS (Figure A3) into the Geant4 application to reproduce the upper third of the spacecraft. With this model, the efficiency of the GRS was characterized for incident angles ranging over $0° < \theta_D < 130°$ in a $2° \times 2°$ grid in θ_D and φ_D space. Figure A4 shows the resulting efficiency map for the 1461-keV gamma ray. Similar maps were created for all of the gamma rays of interest for this study. The attenuation of incident gamma rays is evident in this efficiency map as a reduction in the detection efficiency for incident angles that subtend spacecraft components prior to detection, and the efficiency map traces out the major spacecraft components surrounding the GRS; for example, the adapter ring and sunshade are clearly observed.

A4. Experimentally Measured Efficiency

[53] Sufficient data exist within the GRS data set to plot the background- and altitude-corrected 1779-keV Si gamma-ray count rates as a function of θ_n. The 1779-keV line was used in the place of the 1461-keV line because of the observation that its count rate does not vary substantially over the surface (Figures 5a, 6a, 6b, and 7a). Unlike the ground-calibration experiments and Geant4 simulations,

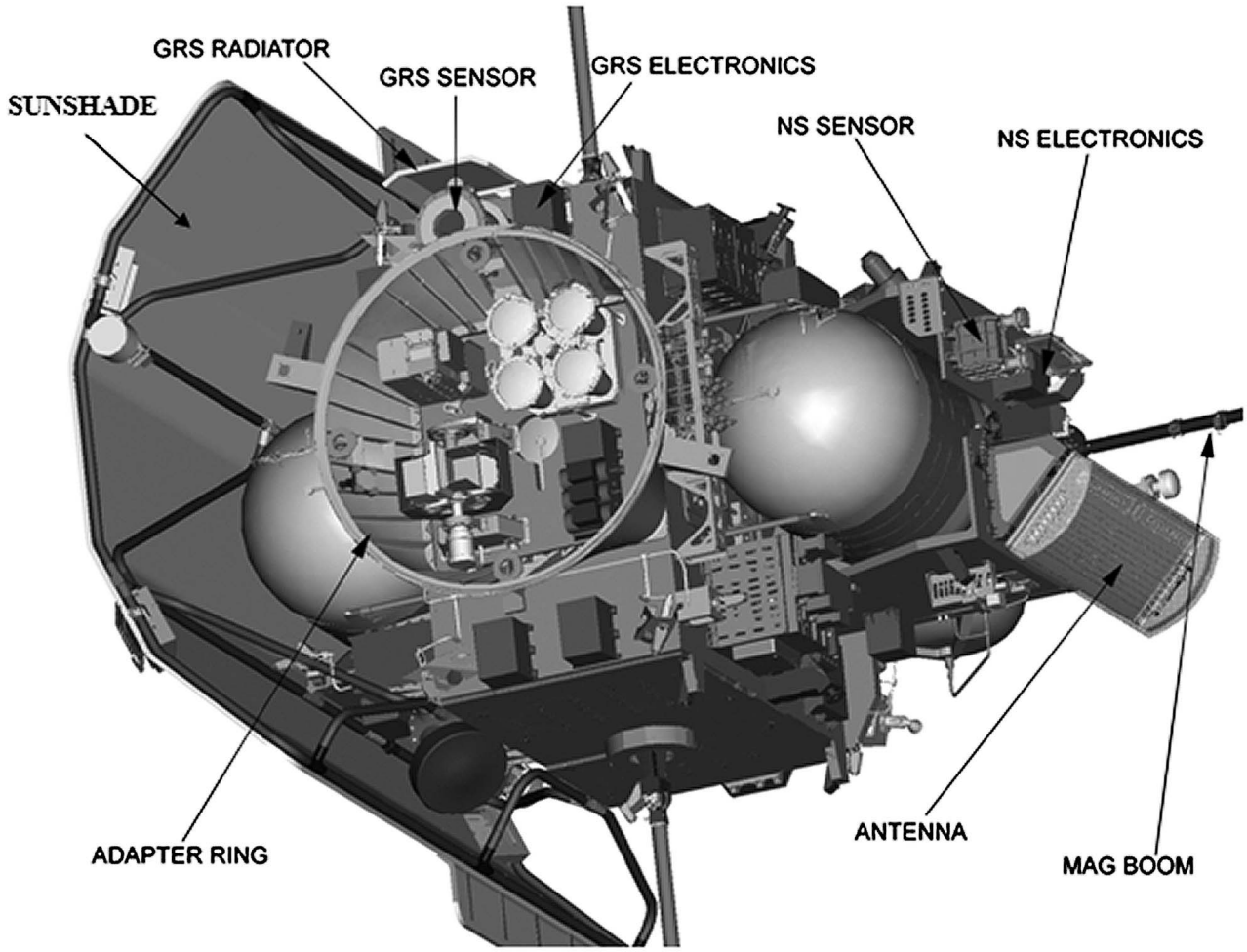

Figure A3. CAD drawing of GRS and NS as positioned on the MESSENGER spacecraft. Only a portion of the 3.6-m boom for MESSENGER's Magnetometer (MAG) is shown. Also indicated are one of MESSENGER's two high-gain phased-array antennas, the carbon fiber sunshade, and the adapter ring by which the spacecraft was mated to the upper stage of the launch vehicle. Figure reproduced from *Rhodes et al.* [2011].

these count rates originate from a large footprint on the surface, and therefore a wide range of θ_D angles. Despite this complication, the relationship between the count rates and θ_n (Figure A5) was found to closely match the relationship expected from the simulations, particularly that the count rate decreases for angles larger than $\sim$45°, which is where the GRS-surrounding spacecraft components begin to attenuate the gamma-ray signal (Figure A4).

A5. GRS Point Response Function

[54] Use of the GRS efficiency maps in the forward code requires a means to properly weigh the relative contribution of any given point on the surface to the total measured gamma-ray count rate in the detector. This weighting was accomplished by utilizing a point response function (PRF) for the footprint of the GRS on the surface. The PRF was derived for an isotropic detector response, a uniform surface composition over the subtended limb solid angle, no atmosphere to attenuate gamma rays, and in the case of non-radioactive elements a constant neutron flux over depths penetrated by gamma rays. The assumption of an isotropic detector response was corrected through the use of the efficiency maps, which describe the non-uniform response of the detector. The PRF is energy-independent and uniform over all azimuth angles (ϕ_D). The PRF for a given point on the surface a distance d along the planet surface from the sub-nadir point is

$$\mathrm{PRF}(d) = \left[\frac{H^2(H - H'c)}{[H^2 + 2H'c]^{3/2}}\right] \tag{A1}$$

where H is h/R_M, H' is $1 + H$, and c is $1 - \cos(d/R_M)$. The distance d is a function of the angle between the sub-nadir point and the surface component of interest, so the PRF for any angle can be calculated. The normalized PRF for each point d along the surface, corresponding to a specific detector-incident angle (θ_D, ϕ_D), was then calculated. The sum of the PRF-weighted detector efficiency at each incident angle multiplied by the altitude-corrected surface flux from

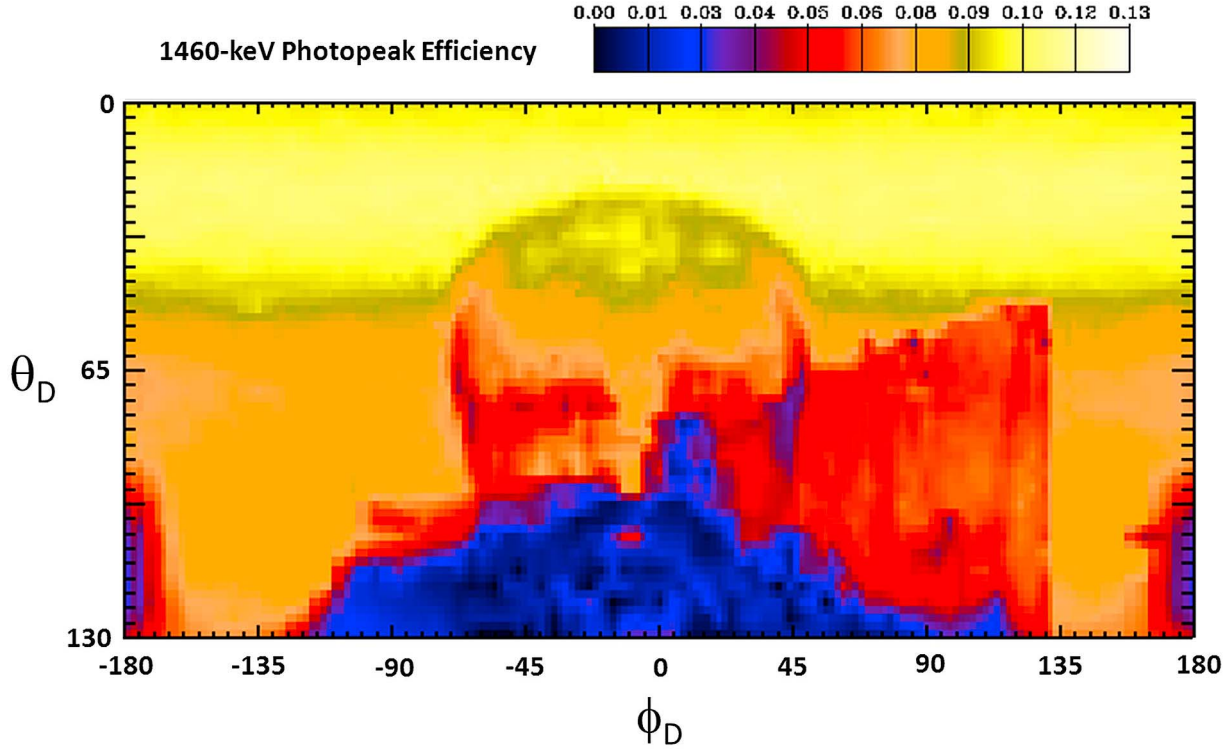

Figure A4. The efficiency of the GRS for detecting 1461-keV gamma rays for all angles $\theta_D \leq 130°$. These values include the intrinsic efficiency of the HPGe sensor as well as the effects of GRS-surrounding spacecraft components, which attenuate the gamma-ray signal prior to detection. GRS-surrounding components such as the sunshade, radiator, and adapter ring (Figure A3) are clearly observed in the efficiency map as regions of decreased detection efficiency. The region of lowest detection efficiencies is in the direction of the spacecraft structure.

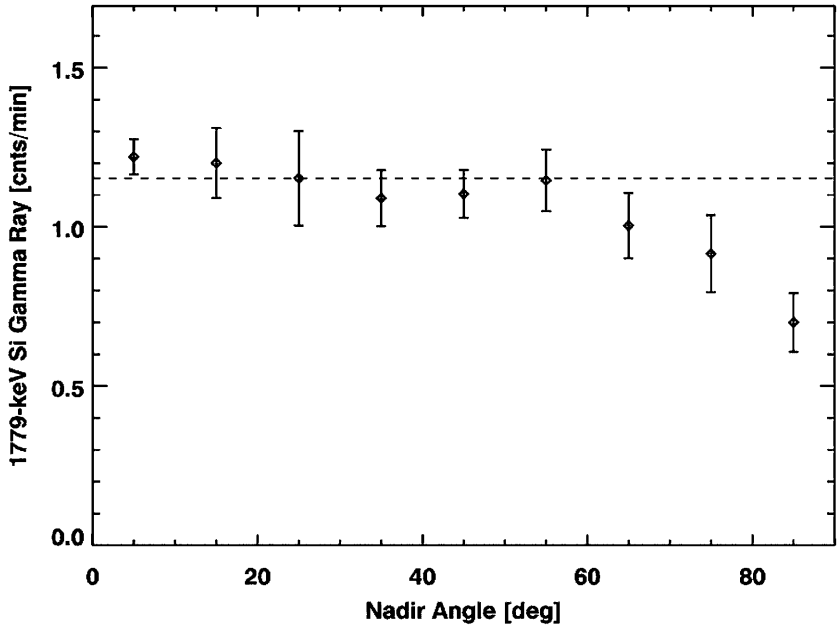

Figure A5. Experimentally measured 1779-keV count rate, corrected for solid angle and background, versus nadir angle. The reduction in the count rate for nadir angles larger than 45° experimentally confirms the simulations (Figure A4), which reveal a reduction in the detector efficiency for these angles. The 1779-keV line was chosen over the 1461-keV line because it does not vary appreciably in strength over the surface (Figure 7).

the corresponding surface element provides the predicted gamma-ray flux at any given altitude.

[55] PRF(d) exhibits the expected behavior, as it is maximum at the sub-nadir point and goes to zero at the limb, where $\cos(d/R_M) = 1/(1 + h/R_M)$. The integral of the PRF over the planet surface is proportional to the solid angle subtended by the planet at altitude h. A comparison of the results of the PRF so calculated to the experimentally determined PRF for the Lunar Prospector GRS at 30 km altitude [*Lawrence et al.*, 2003] and the simulated PRF for the Mars Odyssey GRS at 400 km [*Boynton et al.*, 2007] altitude shows agreements. The PRF also has the expected behavior at large altitudes ($h \gg R_M$), where the subtended solid angle is small and the detector-incident gamma rays are parallel. These tests provided the confidence necessary to utilize this PRF over the full range of altitudes in the low-altitude data set (200–2000 km).

Appendix B: Correlation Between Spacecraft Ephemeris and GRS Measurements

B1. GRS Measurement Geometry

[56] During MESSENGER's primary mission, the spacecraft orbited Mercury in a highly eccentric, near polar orbit with a period of 12 h (see Figure B1a). This orbit, in conjunction with the altitude dependence of the GRS signal (equation (1)), limited the spatial coverage of the GRS measurements to regions north of −20° latitude. This orbit also results in a double-valued correlation between the spacecraft altitude and the sub-nadir latitude (Figure B1b). As a result, the spatial resolution and statistical significance of the measurements have a latitudinal dependence, with higher spatial resolution and sensitivity at northern latitudes. This effect necessitated the use of varying pixel sizes in the K abundance map (Figure 8) in order to maintain low statistical errors for each pixel.

[57] The thermal conditions at the surface, particularly the presence of hot poles at longitudes 0° and 180°, frequently necessitated the use of off-nadir pointing over these regions, which includes the Caloris basin. This off-nadir pointing can potentially impact the measured gamma-ray count rates, as measurements taken at large nadir angles have lower detection efficiencies (see Figures A4 and A5). Our map of K abundances, which has the highest values in the far north and low values over the hot poles, could possibly be attributed to the nature of the MESSENGER orbit and spacecraft attitude if the data were not properly corrected.

[58] Evidence that these observational biases have not influenced the results comes from two sources. The first is the 1779-keV Si and 6129-keV O gamma-ray count rate maps. These gamma rays, particularly the 1779-keV line, are subject to the same measurement correlations as the 1461-keV K gamma ray. The uniform count rate maps for the 1779-keV and 6129-keV gamma rays are taken as evidence that the corrections described here have fully removed the effects of the measurement correlations from this analysis, on the grounds that correlations would otherwise be observed between these gamma rays and spacecraft attitude for each pixel. The second piece of evidence comes from plotting the K abundance versus the measurement time, average nadir angle, and average altitude for each pixel. In all cases, no correlation was found between the derived K abundance and the measurement parameter.

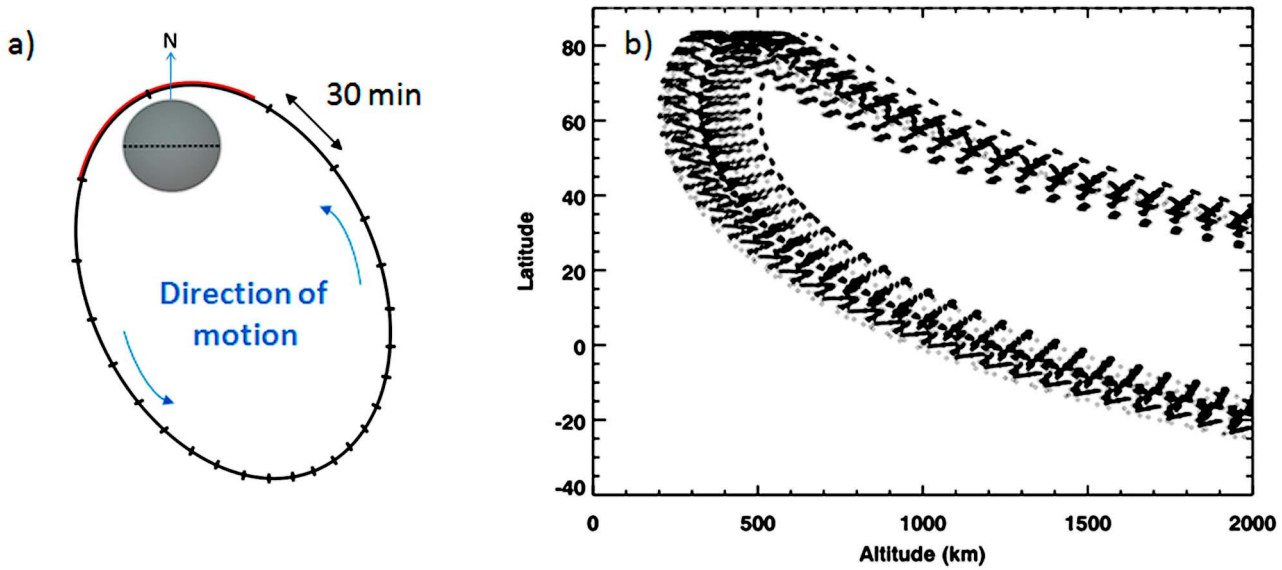

Figure B1. (a) The near-polar, highly eccentric orbit of the MESSENGER spacecraft during its primary mission, with tick marks at 30-min time intervals and blue arrows indicating the direction of spacecraft motion. The orbit ranges from a minimum periapsis altitude of 200 km to a maximum apoapsis altitude of 15,500 km. The red highlighted segment of the orbit illustrates the low-altitude (<2000 km) portion. (b) The latitude of the spacecraft as a function of altitude for all data acquired from 24 March to 28 September 2011. There are two branches in this representation of the orbit, which results in a latitude-dependent signal strength and spatial resolution.

Appendix C: Gamma-Ray Background Signals

C1. Types of Backgrounds in the GRS

[59] There are five possible sources of discrete-energy gamma ray photopeaks in GRS spectra: the decay of radioactive elements on the spacecraft (S_R), prompt gamma-ray emission by the excitation of spacecraft materials by spacecraft-incident GCRs (S_B), delayed gamma-ray emission resulting from long-lived activation of spacecraft materials by spacecraft-incident GCRs or solar-originating energetic particles (S_A), excitation of spacecraft materials by spacecraft-incident, planet-originating neutrons (S_N), and finally the planet-originating gamma rays of interest (S_P), where S represents the measured count rates from each of these sources. The components S_R, S_B, S_A, and S_N are sources of background, and S_P is used to measure the elemental composition of the surface. Contributions to the measured gamma-ray signals from each of the background sources must be carefully removed in order to determine the magnitude of the signal originating from the surface.

C2. Background Removal

[60] The decay of radioactive elements on the spacecraft (S_R) is observed in the GRS as the result of K, Th, and U contamination in spacecraft materials. Since the long-lived radioactive isotopes of each of these elements has a half-life $t_{1/2}$ of 10^9 years or more, their backgrounds are treated as constant over the life of the mission. S_R for each photopeak

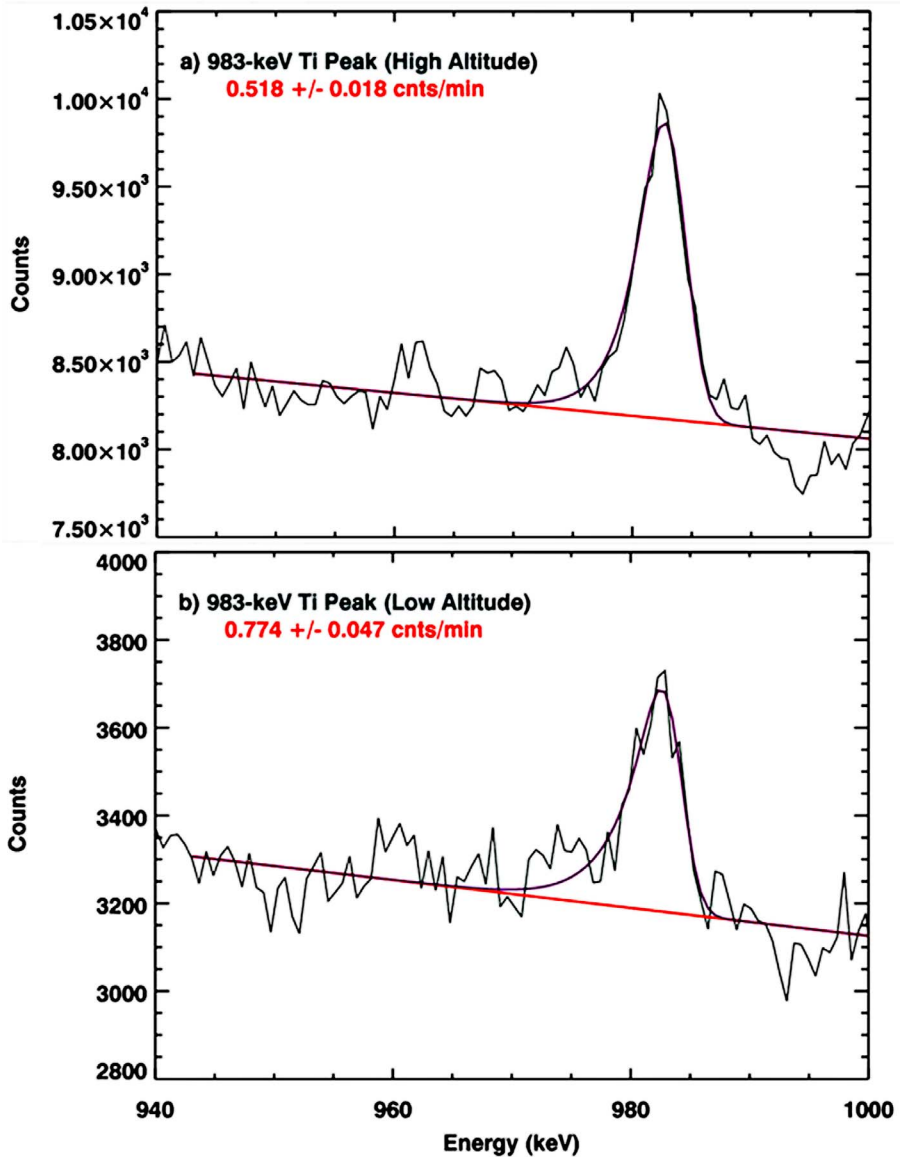

Figure C1. (a) High-altitude and (b) low-altitude fits to the 983-keV Ti peak used to determine the background amplification factor. The fits utilize near-nadir (<15°) data from the first 59 days of orbital operations, ensuring complete coverage of the surface as well as limiting contributions from time-dependent variations in the spacecraft-incident GCR flux and spacecraft activation from solar energetic particles events (e.g., 4 June 2011).

can therefore be quantified from high-altitude data, beyond the range of detection for planet-originating signals (see Table 3). As S_N, S_B, and S_A are not present for radioactive elements, S_P is determined by simply subtracting S_R from the low-altitude measurement of interest.

[61] Stable elements are subject to backgrounds from S_N, S_B, and S_A. One of these backgrounds, S_B, can be removed using geometric information. S_B is a function of the spacecraft-incident GCR flux and therefore depends on both altitude and time. The altitude variations are due to occultation of GCRs by Mercury, and the time dependency is the result of variations in the GCR flux in response to varying solar conditions (e.g., *McKinney et al.* [2006] and discussion in section 3.3). The altitude dependence of S_B is characterized as

$$S_B(h) = S_B(\infty) \cdot [1 - \Omega(h)] \quad \text{(C1)}$$

where $\Omega(h)$ is the fractional solid angle of the planet as viewed by the GRS (see section 3.4). As $\Omega(h)$ describes the fraction of the 4π-sr field of view of the GRS that is filled by its horizon-to-horizon view of the surface, $1\text{-}\Omega(h)$ describes the fraction that is unobstructed by Mercury, and by extension the fraction of the total GCR flux that has access to the spacecraft. $S_B(\infty)$ is quantified with the GRS data acquired near apoapsis (~15,500 km, Table 3), where $\Omega(h) \rightarrow 0$. The altitude-dependent model for $S_B(h)$ (equation (C1)) allows for the removal of $S_B(h)$ from the measured gamma-ray signal.

[62] Measurements of stable elements can also be contaminated by S_A, which describes the long-lived activation of spacecraft components by incident particles. S_A is dominated by contributions from spacecraft-incident solar flares, which under certain conditions can produce activation products in the spacecraft (e.g., $^{56}Fe(p, n)^{56}Co$, $t_{1/2}$ = 77.2 d, and $^{48}Ti(p, n)^{48}V$, $t_{1/2}$ = 15.9 d). Contributions from S_A are negated by omitting flare-compromised data from the analysis of elemental abundances when such activation products are present (Evans et al., submitted, 2012). However, S_A does not contribute to the Si and O gamma rays examined here.

[63] The final source of background signal for the stable elements is the excitation of spacecraft materials by planet-originating neutrons (S_N). S_N has the same altitude-dependence (equation (1)) as S_P when it originates from inelastic scattering, as is the case for the Si and O gamma rays examined here. S_N originating from neutron capture is complicated by the fact that thermal neutrons are gravitationally bound to Mercury and thus have a different altitude dependence than those originating from inelastic scattering. The fact that the inelastic scattering S_N backgrounds have the same altitude dependence as the signal of interest prevent utilizing the spacecraft ephemeris to remove the background from the measured signal, as was done for S_B (equation (C1)). Under certain circumstances, S_N can be removed by utilizing knowledge of the nuclear reaction cross sections for the elements under consideration (Peplowski et al., submitted, 2012), but for this analysis S_N was not removed from the data prior to analysis.

[64] The presence of S_N in the Si and O results presented here suggests the possibility that these results are dominated by spacecraft backgrounds. An early attempt to characterize S_N was carried out by *Rhodes et al.* [2011], who defined the background amplification factor (A_{BG}) to be the ratio of the low- to high-altitude count rates in the 1014-keV Al inelastic scattering peak. This peak was chosen because it was assumed, as a result of the large amount of Al surrounding the HPGe, that the measured Al peaks would be dominated by spacecraft-originating background. In the formalism presented here, this assumption would correspond to

$$A_{BG} = \frac{[S_P + S_N + S_B]^{LA}}{[S_B]^{HA}} \rightarrow \frac{S_N^{LA}}{S_B^{HA}} \quad \text{(C2)}$$

where HA and LA are the high- and low-altitude data selections, and $(S_P + S_N + S_B)^{LA} \rightarrow S_N^{LA}$ on the basis of the fact that $S_B^{LA} \ll (S_P + S_N)^{LA}$ (see Table 3) and the assumption that $S_N^{LA} \gg S_P^{LA}$ for gamma rays from Al [*Rhodes et al.*, 2011]. Analysis of the Al peak provided a background amplification factor of 2.10 ± 0.49. A more rigorous examination of the Al backgrounds (Peplowski et al., submitted, 2012) revealed that for Al, $S_P^{LA} \approx S_N^{LA}$, and therefore a value of 2.10 overestimates the background amplification factor.

[65] On the basis of MESSENGER X-Ray Spectrometer measurements indicating that abundances of Ti on the surface of Mercury are low [*Nittler et al.*, 2011], the 983-keV Ti peak meets the requirement of $S_N^{LA} \gg S_P^{LA}$ and was therefore used to determine an improved background amplification factor. Analysis of this peak (Figure C1) yields an amplification factor of 1.49 ± 0.10. Application of this background amplification factor provides $S_N = A_{BG} \times S_B$ values of 0.228 ± 0.029 and 0.434 ± 0.035 counts per minute for Si and O, respectively. These values correspond to S_N/S_P = 0.12 (Si) and S_N/S_P = 0.32 (O), which suggest that our Si and O count rate maps are derived primarily from signals from the planet, but those signals are mixed with nonzero background contributions.

[66] The background amplification factor method relies on the assumption that the value derived from the 983-keV Ti gamma ray is applicable to other elements. Since the inelastic scattering cross sections depend on the specific isotope in question as well as the energy of the gamma ray of interest, this assumption must be tested. Cross-section data for Ti, Si, and O were retrieved from the Evaluated Nuclear Data File (ENDF) [*Chadwick et al.*, 2011] database for the inelastic scattering reactions leading to the production of 983-keV Ti, 1779-keV Si, and 6129-keV O gamma rays. A comparison of the cross sections reveals that they are of similar magnitude, so the use of the Ti gamma ray to quantify the change in the Si and O gamma-ray backgrounds is valid. It should be noted that because the Ti line is of lower energy than the Si and O gamma rays of interest, it samples the neutron flux at lower energies. Since the neutron flux from the planet decreases with increasing energy [e.g., *Feldman et al.*, 1998], the 983-keV-derived amplification factor is an upper limit, and the actual values of S_N will be smaller, particularly for the 6129-keV O gamma ray.

[67] **Acknowledgments.** We thank D. A. Paige for providing the modeled surface temperatures utilized in this study and G. J. Taylor for providing the Martian K and Th abundances for comparison with these results. We also thank two anonymous reviewers for thoughtful reviews that improved the clarity of the text. Finally, we are indebted to the entire MESSENGER team for their invaluable contributions to the development

and operation of the MESSENGER spacecraft. The MESSENGER mission is supported by the NASA Discovery Program under contract NAS5-97271 to The Johns Hopkins University Applied Physics Laboratory and NASW-00002 to the Carnegie Institution of Washington.

References

Agostinelli, S., and the GEANT4 Collaboration (2003), GEANT4–A simulation toolkit, *Nucl. Instrum. Methods Phys. Res., Sect. A*, *506*, 250–303, doi:10.1016/S0168-9002(03)01368-8.

Blewett, D. T., et al. (2011), Hollows on Mercury: MESSENGER evidence for geologically recent volatile-related activity, *Science*, *333*, 1856–1859, doi:10.1126/science.1211681.

Boynton, W. V., et al. (2007), Concentration of H, Si, Cl, K, Fe, and Th in the low- and mid-latitude regions of Mars, *J. Geophys. Res.*, *112*, E12S99, doi:10.1029/2007JE002887.

Chadwick, M. B., et al. (2011), ENDF/B-VII.1 nuclear data for science and technology: Cross sections, covariances, fission product yields and decay data, *Nucl. Data Sheets*, *112*, 2887–2996, doi:10.1016/j.nds.2011.11.002.

Colombo, G., and I. I. Shapiro (1966), The rotation of planet Mercury, *Astrophys. J.*, *145*, 296–307, doi:10.1086/148762.

Denevi, B. W., et al. (2009), The evolution of Mercury's crust: A global perspective from MESSENGER, *Science*, *324*, 613–618, doi:10.1126/science.1172226.

Domingue, D. L., P. L. Koehn, R. M. Killen, A. L. Sprague, M. Sarantos, A. F. Cheng, E. T. Bradley, and W. E. McClintock (2007), Mercury's atmosphere: A surface-bounded exosphere, *Space Sci. Rev.*, *131*, 161–186, doi:10.1007/s11214-007-9260-9.

Doressoundiram, A., F. Leblanc, A. Gicquel, G. Cremonese, J.-F. Donati, and C. Veillet (2010), Spatial variations of the sodium/potassium ratio in Mercury's exosphere uncovered by high-resolution spectroscopy, *Icarus*, *207*, 1–8, doi:10.1016/j.icarus.2009.11.020.

Evans, L. G., R. C. Reedy, R. D. Starr, K. E. Kerry, and W. V. Boynton (2006), Analysis of gamma ray spectra measured by Mars Odyssey, *J. Geophys. Res.*, *111*, E03S04, doi:10.1029/2005JE002657.

Feldman, W. C., S. Maurice, A. B. Binder, B. L. Barraclough, R. C. Elphic, and D. J. Lawrence (1998), Fluxes of fast and epithermal neutrons from Lunar Prospector: Evidence for water ice at the lunar poles, *Science*, *281*, 1496–1500, doi:10.1126/science.281.5382.1496.

Feldman, W. C., et al. (2010), Evidence for extended acceleration of solar flare ions from 1–8 MeV solar neutrons detected with the MESSENGER Neutron Spectrometer, *J. Geophys. Res.*, *115*, A01102, doi:10.1029/2009JA014535.

Felinger, A. (1994), Deconvolution of overlapping skewed peaks, *Anal. Chem.*, *66*, 3066–3072, doi:10.1021/ac00091a013.

Giletti, B. J., and T. M. Shanahan (1997), Alkali diffusion in plagioclase feldspar, *Chem. Geol.*, *139*, 3–20, doi:10.1016/S0009-2541(97)00026-0.

Goldreich, P., and S. Peale (1966), Spin-orbit coupling in the solar system, *Astron. J.*, *71*, 425–438, doi:10.1086/109947.

Goldsten, J. O., et al. (2007), The MESSENGER Gamma-Ray and Neutron Spectrometer, *Space Sci. Rev.*, *131*, 339–391, doi:10.1007/s11214-007-9262-7.

Head, W. J., et al. (2008), Volcanism on Mercury: Evidence from the first MESSENGER flyby, *Science*, *321*, 69–72, doi:10.1126/science.1159256.

Head, J. W., et al. (2011), Flood volcanism in the northern high latitudes of Mercury revealed by MESSENGER, *Science*, *333*, 1853–1856, doi:10.1126/science.1211997.

Hörz, F., R. Grieve, G. Heiken, P. Spudis, and A. Binder (1991), Lunar surface processes, in *Lunar Sourcebook: A User's Guide to the Moon*, edited by G. Heiken, D. Vaniman, and B. M. French, pp. 61–111, Cambridge Univ. Press, New York.

Killen, R. M., M. Sarantos, A. E. Potter, and P. Reiff (2004), Source rates and ion recycling rates for Na and K in Mercury's atmosphere, *Icarus*, *171*, 1–19, doi:10.1016/j.icarus.2004.04.007.

Killen, R. M., et al. (2007), Processes that promote and deplete the exosphere of Mercury, *Space Sci. Rev.*, *132*, 433–509, doi:10.1007/s11214-007-9232-0.

Kobayashi, S., et al. (2010), Determining the absolute abundances of natural radioactive elements on the lunar surface by the Kaguya Gamma-ray Spectrometer, *Space Sci. Rev.*, *154*, 193–218, doi:10.1007/s11214-010-9650-2.

Korotev, R. L. (1998), Concentrations of radioactive elements in lunar materials, *J. Geophys. Res.*, *103*, 1691–1701, doi:10.1029/97JE03267.

Lawrence, D. J., R. C. Elphic, W. C. Feldman, T. H. Prettyman, O. Gasnault, and S. Maurice (2003), Small-area thorium features on the lunar surface, *J. Geophys. Res.*, *108*(E9), 5102, doi:10.1029/2003JE002050.

Lawrence, D. J., S. Maurice, and W. C. Feldman (2004), Gamma-ray measurements from Lunar Prospector: Time series data reduction from the Gamma-Ray Spectrometer, *J. Geophys. Res.*, *109*, E07S05, doi:10.1029/2003JE002206.

Leblanc, F., and A. Doressoundiram (2011), Mercury exosphere. II. The sodium/potassium ratio, *Icarus*, *211*, 10–20, doi:10.1016/j.icarus.2010.09.004.

Lodders, K., and B. Fegley Jr. (1998), *The Planetary Scientist's Companion*, Oxford Univ. Press, New York.

Markwardt, C. B. (2009), Non-linear least squares fitting in IDL with MPFIT, in *Proceedings of the Astronomical Data Analysis Software and Systems XVIII*, *ASP Conf. Ser.*, vol. 441, edited by D. Bohlender, P. Doweler, and D. Durand, pp. 251–254, Astron. Soc. of the Pac., San Francisco, Calif.

Maurice, S., D. J. Lawrence, W. C. Feldman, R. C. Elphic, and O. Gasnault (2004), Reduction of neutron data from Lunar Prospector, *J. Geophys. Res.*, *109*, E07S04, doi:10.1029/2003JE002208.

McCubbin, F. M., M. A. Riner, K. E. Nader Kaaden, and L. K. Burkemper (2012), Is Mercury a volatile-rich planet?, *Geophys. Res. Lett.*, *39*, L09202, doi:10.1029/2012GL051711.

McKinney, G. W., D. J. Lawrence, T. H. Prettyman, R. C. Elphic, W. C. Feldman, and J. J. Hagerty (2006), MCNPX benchmark for cosmic ray interactions with the Moon, *J. Geophys. Res.*, *111*, E06004, doi:10.1029/2005JE002551.

Moré, J. (1978), The Levenberg-Marquardt algorithm: Implementation and theory, in *Numerical Analysis, Lecture Notes Math.*, vol. 630, edited by G. A. Watson, pp. 105–116, Springer, Berlin.

Nittler, L. R., et al. (2011), The major element composition of Mercury's surface from MESSENGER X-ray spectrometry, *Science*, *333*, 1847–1850, doi:10.1126/science.1211567.

Peplowski, P. N., D. T. Blewett, B. W. Denevi, L. G. Evans, D. J. Lawrence, L. R. Nittler, E. A. Rhodes, C. M. Selby, and S. C. Solomon (2011a), Mapping iron abundances on the surface of Mercury: Predicted spatial resolution of the MESSENGER Gamma-Ray Spectrometer, *Planet. Space Sci.*, *59*, 1654–1658, doi:10.1016/j.pss.2011.06.001.

Peplowski, P. N., et al. (2011b), Radioactive elements on Mercury's surface from MESSENGER: Implications for the planet's formation and evolution, *Science*, *333*, 1850–1852, doi:10.1126/science.1211576.

Potter, A. E., and T. H. Morgan (1986), Potassium in the atmosphere of Mercury, *Icarus*, *67*, 336–340, doi:10.1016/0019-1035(86)90113-2.

Potter, A. E., and T. H. Morgan (1997), Sodium and potassium atmospheres of Mercury, *Planet. Space Sci.*, *45*, 95–100, doi:10.1016/S0032-0633(96)00100-6.

Pourrouquet, P., J.-C. Thomas, P.-F. Peyard, R. Ecoffet, and R. Rolland (2011), FASTRAD 3.2: Radiation shielding tool with a new Monte Carlo module, in *2011 Radiation Effects Data Workshop*, pp. 200–204, IEEE, Piscataway, N. J., doi:10.1109/REDW.2010.6062530.

Prettyman, T. H., J. J. Hagerty, R. C. Elphic, W. C. Feldman, D. J. Lawrence, G. W. McKinney, and D. T. Vaniman (2006), Elemental composition of the lunar surface: Analysis of gamma ray spectroscopy data from Lunar Prospector, *J. Geophys. Res.*, *111*, E12007, doi:10.1029/2005JE002656.

Reedy, R. C. (1978), Planetary gamma-ray spectroscopy, *Proc. Lunar Planet. Sci. Conf.*, *9th*, 2961–2984.

Rhodes, E. A., et al. (2011), Analysis of MESSENGER Gamma-Ray Spectrometer data from the Mercury flybys, *Planet. Space Sci.*, *59*, 1829–1841, doi:10.1016/j.pss.2011.07.018.

Solomon, S. C., R. L. McNutt Jr., R. E. Gold, and D. L. Domingue (2007), MESSENGER mission overview, *Space Sci. Rev.*, *131*, 3–39, doi:10.1007/s11214-007-9247-6.

Soter, S. L., and J. Ulrichs (1967), Rotation and heating of the planet Mercury, *Nature*, *214*, 1315–1316, doi:10.1038/2141315a0.

Sprague, A. L. (1990), A diffusion source for sodium and potassium in the atmospheres of Mercury and the Moon, *Icarus*, *84*, 93–105, doi:10.1016/0019-1035(90)90160-B.

Sprague, A. L. (1992), Mercury's atmospheric bright spots and potassium variations: A possible cause, *J. Geophys. Res.*, *97*, 18,257–18,264, doi:10.1029/92JE01690.

Sprague, A. L., R. W. H. Kozlowski, and D. M. Hunten (1990), Caloris basin: An enhanced source for potassium in Mercury's atmosphere, *Science*, *249*, 1140–1143, doi:10.1126/science.249.4973.1140.

Sprague, A. L., K. L. Donaldson Hanna, R. W. Kozlowski, J. Helbert, A. Maturilli, J. B. Warell, and J. L. Hora (2009), Spectral emissivity measurements of Mercury's surface indicate Mg- and Ca-rich mineralogy, K-spar, Na-rich plagioclase, rutile, with possible perovskite, and garnet, *Planet. Space Sci.*, *57*, 364–383, doi:10.1016/j.pss.2009.01.006.

Surkov, Y. A., F. F. Kirnozov, V. N. Glazov, A. G. Dunchenko, L. P. Tatsy, and O. P. Sobornov (1987), Uranium, thorium, and potassium in the Venusian rocks at the landing sites of Vega 1 and 2, *J. Geophys. Res.*, *92*, E537–E540, doi:10.1029/JB092iB04p0E537.

Taylor, G. J., and E. R. D. Scott (2003), Mercury, in *Meteorites, Comets, and Planets, Treatise on Geochemisty*, vol. 1, edited by A. M. Davis, pp. 477–485, Elsevier-Pergamon, Oxford, U. K.

Taylor, G. J., et al. (2006), Bulk composition and early differentiation of Mars, *J. Geophys. Res.*, *111*, E03S10, doi:10.1029/2005JE002645.

Vasavada, A. R., D. A. Paige, and S. E. Wood (1999), Near-surface temperatures on Mercury and the Moon and the stability of polar ice deposits, *Icarus*, *141*, 179–193, doi:10.1006/icar.1999.6175.

Watters, T. R., S. L. Murchie, M. S. Robinson, S. C. Solomon, B. W. Denevi, S. L. André, and J. W. Head (2009), Emplacement and tectonic deformation of smooth plains in the Caloris basin, Mercury, *Earth Planet. Sci. Lett.*, *285*, 309–319, doi:10.1016/j.epsl.2009.03.040.

Weider, S. Z., L. R. Nittler, R. D. Starr, T. J. McCoy, K. R. Stockstill-Cahill, P. K. Byrne, J. W. Head, and S. C. Solomon (2012), Chemical heterogeneity on Mercury's surface revealed by the MESSENGER X-Ray Spectrometer, *J. Geophys. Res.*, doi:10.1029/2012JE004153, in press.